CORA Cork Open Research Archive
Cartlann Taighde Oscailte Chorcaí

Title	A statistical re-examination of the spoiled gradient recall echo equation in the analysis of data from DSC and DCE MR imaging procedures
Authors	Hu, Yuankun
Publication date	2025
Original Citation	Hu, Y. 2025. A statistical re-examination of the spoiled gradient recall echo equation in the analysis of data from DSC and DCE MR imaging procedures. PhD Thesis, University College Cork.
Type of publication	Doctoral thesis
Rights	© 2025, Yuankun Hu. - https://creativecommons.org/licenses/by/4.0/
Download date	2026-11-03 03:45:20
Item downloaded from	https://hdl.handle.net/10468/18477

UCC
University College Cork, Ireland
Coláiste na hOllscoile Corcaigh

A Statistical Re-Examination of the Spoiled Gradient Recall Echo Equation in the Analysis of Data from DSC and DCE MR Imaging Procedures

Yuankun Hu

Thesis submitted for the degree of
Doctor of Philosophy



NATIONAL UNIVERSITY OF IRELAND, CORK
SCHOOL OF MATHEMATICAL SCIENCES

October 2025

Head of School: Dr. Martin Kilian
Supervisors: Prof. Finbarr O'Sullivan
Dr. Jian Huang

Contents

List of Figures **v**

List of Tables **xix**

Acknowledgements **xxiii**

Abstract **xxv**

1 Overview of Thesis **1**

1.1 Introduction 1

1.2 Main Contributions 3

1.3 Thesis Structure 4

2 Background of MRI **7**

2.1 Medical Imaging 8

2.2 Magnetic Resonance Imaging 10

2.2.1 Development of MR Scanners 10

2.2.2 Mechanism of MRI 13

2.2.3 Image Reconstruction 22

2.3 Spoiled-GRE Equation 26

2.4 Perfusion MR Imaging 27

2.4.1 DSC-MRI 27
2.4.2 DCE-MRI 28
2.4.3 ASL-MRI 29
2.5 Contrast Agents 32
2.6 Advantages and Disadvantages of MRI 33

3 Reconstructing Contrast Agent Concentration from MR Signal 35
3.1 Signal Conversion Methods 36
3.1.1 DSC-MR Images 37
3.1.2 DCE-MR Images 39
3.2 Artifacts 44
3.2.1 Artifacts in DSC-MR Images 48
3.2.2 Artifacts in DCE-MR Images 55
3.3 Two-Parameter Method 62
3.3.1 Parameter Optimisation 64
3.4 Unique Recovery 67
3.4.1 Demonstration of Unique Recovery of Parameters with DSC Data 68
3.4.2 Demonstration of Unique Recovery of Parameters with DCE Data 72
3.5 Numerical Simulation 74
3.5.1 Simulation with DSC-MR Data 76
3.5.2 Simulation with DCE-MR Data 86
3.6 Other Artifacts 93
3.7 Conclusion 94

4 Pharmacokinetic Modelling **97**

4.1 Modelling in DSC-MRI 98

4.1.1 Semi-quantitative Method 98

4.1.2 Quantitative Methods 101

4.1.3 Corrections in Concentration of DSC-MRI 105

4.1.4 Summary of DSC-MRI Analysis 109

4.2 Modelling for DCE-MRI 110

4.2.1 Semi-quantitative Method 110

4.2.2 Quantitative Models 112

4.2.3 Compartmental Models 113

4.2.4 Summary of DCE-MRI Analysis 125

4.3 Common Goal in Quantitative Analysis 127

4.4 Conclusion 128

5 Comparison of the Conventional and Proposed Models on Clinical Dataset **131**

5.1 The Standard Approaches 132

5.2 The Proposed Model 134

5.3 MRI Data Acquisition 137

5.4 Comparative Analysis 141

5.4.1 DSC-MRI Comparison 143

5.4.2 DCE-MRI Comparison 154

5.5 Conclusion 163

6 Discussion and Future Work **165**

6.1 Discussion 167

6.2 Future Work 169

References **171**

A List of Publications by the Author **A197**

A.1 Conferences Presentations A197

B Nomenclature **B199**

B.1 Symbol Definitions B199

B.2 Abbreviations B202

List of Figures

2.1 The sagittal brain images from X-Ray, CT, PET, and MRI (Kshatri et al. 2023). 9

2.2 Scheme of MRI: (a) magnet coil to produce B_0; (b) gradient coil to produce time-varying gradient fields; (c) RF coil to generate B_1 (Moser et al. 2009). 14

2.3 The mechanism of MRI: the picture in the top left presents protons that are randomly oriented in the body without a magnetic field. When a magnetic field is applied, most of the protons align with the direction of the magnetic field B_0, as seen in the top right. Once an RF is emitted, the protons tilt sideways (bottom left) and they return to their original alignment as the RF is turned off (bottom right). 15

2.4 The T_1 relaxation time: an exponential recovery of longitudinal magnetization (M_z) following the application of a 90° RF pulse at equilibrium. After excitation, M_z gradually returns toward its baseline value (Tadanki 2018). 17

2.5 The T_2 and T_2^* relaxation time: following the application of a 90° RF pulse at time t, transverse magnetisation undergoes exponential decay. The dark grey curve represents the T_2 relaxation, while the dark red curve represents the more rapid T_2^* decay, known as FID (Chavhan et al. 2009). 18

2.6 The multiple echoes produced by RF pulse sequences (Chow et al. 2022). 19

2.7 Relationship between MR signal intensity, RF, TE, and TR (Shamir et al. 2025). 20

2.8 Generation procedure of GRE sequences (Selvakumar et al. 2014). 21

2.9 A procedure of MR image reconstruction. MR imaging begins with signal encoding performed by the scanner hardware, which includes RF transmission/reception and spatial gradients. The encoded signals are sampled and mapped into k-space. Finally, a Fourier transform is applied to reconstruct images from the k-space data. 23

2.10 k-space (left) and its associated image (right) of a patient with transposition of great vessels. Each point in k-space contributes to the entire image, and conversely, each pixel in the image is influenced by all points in k-space, reflecting their Fourier relationship (Moratal et al. 2008). 25

2.11 A gadolinium-based contrast (gadoteridol with empirical formula of $C_{17}H_{29}N_4O_7Gd$) manufactured by Bracco Diagnostics Inc. . . . 32

3.1 In DSC-MRI, the relative signal intensity (a) has a maximum value of 1, and its corresponding concentration (b) is obtained through negative logarithmic transformation. 39

3.2 The change in maximum relative signal with increasing B. The x-axis is $B = exp(-TR/T_{10})$, and the y-axis represents maximum relative signal intensity in DSC-MRI. 49

3.3 Examine the artifact in signal reconstruction in DSC-MRI. 50

3.4 A scaled concentration profile ($ci(t)$) from a normal region of a brain tumour patient. The baseline period has been removed, consistent with all subsequent time courses presented in this thesis. 51

3.5 Comparison of concentration before and after reconstruction. The black curves are $C_t(t)$ and green curves represent $\hat{C}_t(t)$, which are reconstructed via $g(u_t)$ in Equation 3.12. The subtitles of each plot are T_{10} and β used to reconstruct $S(t)/S_0$. 52

3.6 Comparison of relative signal intensity. The black curves are $S(t)/S_0$ and the blue curves represent $\hat{S}(t)/\hat{S}_0$, which are reconstructed through the spoiled-GRE equation. The subtitles of each plot are T_{10} and β used to reconstruct $S(t)/S_0$. 53

3.7 Segmented relative signal intensity in DSC-MR image and corresponding regions in the middle slice. 54

3.8 The variation in maximum relative signal as B increases. The x-axis is $B = exp(-TR/T_{10})$, while the y-axis corresponds to the maximum relative signal intensity $S(t)/S_0$. 57

3.9 Comparison of concentration before and after reconstruction. The black curves are $C_t(t)$ and green curves represent $\hat{C}_t(t)$, which are reconstructed via $f(u_t)$ in Equation 3.12. The subtitles of each plot are T_{10} and β used to reconstruct $S(t)/S_0$. 59

3.10 Comparison of relative signal intensity. The black curves are $S(t)/S_0$ and the blue curves represent $\hat{S}(t)/\hat{S}_0$, which are reconstructed through the spoiled-GRE equation. The subtitles of each plot are T_{10} and β used to reconstruct $S(t)/S_0$. 60

3.11 Segmented relative signal intensity in DCE-MR image and corresponding regions in the middle slice. 61

3.12 Process of the two-parameter method. The $\Delta R_2^*(t)$ and $E(t)$ are considered as concentration profiles $ci(t)$ for DSC- and DCE-MR images, respectively. The RSS image demonstrates all RSS values, with a colour transition from red to blue indicating a gradual decrease. The optimised parameter $\hat{\alpha}$ and $\hat{\beta}$ are determined at the minimum RSS. 66

3.13 A process for generating $(S(t)/S_0)^*$. The $ci(t)$ is a Gamma density function and is normalised to 1. Based on Equation 3.13, the true $(S(t)/S_0)^*$ can be computed using the true values of α^* and β^*. . . 69

3.14 A process to generate $\hat{S}(t)/\hat{S}_0$. Different colours and profiles in $\hat{S}(t)/\hat{S}_0$ represent different combinations of α_j and β_j. 70

3.15 In image (a), the white dot represents RSS of α^* and β^* while the black asterisk represents RSS of a specific combination of α_j and β_j. The plots (b) and (c) demonstrate the minimum RSS, which occurs when the ratio is equal to 1. 70

3.16 Enhanced relative signal intensities in T_2-weighted domain. . . . 71

3.17 The image (a) presents the RSS values. The white dot represents the minimum RSS, and the black asterisk represents the RSS of a specific combination of α_j and β_j. The plots (b) and (c) display the RSS values as functions of the ratios α_j/α^* and β_j/β^*, respectively, with the minimum RSS occurring precisely at a ratio of 1. 72

3.18 Enhanced (upper) and susceptibility (bottom) relative signal intensities in DCE-MR domain. 73

3.19 Proof of identifiability in DCE-MR images. 74

3.20 The 10^{th} slice of DSC-MR image of the patient at the middle time frame. The orange region on the top right represents the tumour, and the green region in the centre is the CSF. The area enclosed by an ellipse represents the ROI and is considered a normal region. 75

3.21 The averaged relative signal intensity and normalised concentration in the normal brain region. 76

3.22 Diagram of Simulation Process. 78

3.23 Simulation result of normal T_2^* effect. The black curves represent theoretical signal intensity $\tilde{S}(t)/\tilde{S}_0$, the red curves represent the true signal intensity $S(t)/S_0$, and the green curves represent estimated signal intensity $\hat{S}(t)/\hat{S}_0$. The blue dots represent the residuals between $S(t)/S_0$ and $\hat{S}(t)/\hat{S}_0$, offset by 1 for better visualisation. The title of each subplot indicates the corresponding noise level σ_s for the current simulation. 79

3.24 The RSS image of $S(t)/S_0$ and $\hat{S}(t)/\hat{S}_0$. The blue dot represents RSS of the initial value of optimisation, and the pink dot shows RSS of true values ($\alpha = 0.980$ and $\beta = 0.5$). The white dot represents the minimum RSS, which matches the RSS of the estimates, showing as a black asterisk. The enlarged window at the bottom right highlights this overlap between the white dot and the black asterisk, with the pink dot located in close proximity. 80

3.25 The red dashed lines in these boxplots represent the true values, $\alpha = 0.98$, $\beta = 0.5$, respectively. The x-axis represents different noise levels. 81

3.26 The x-axis represents different noise levels and the y-axis in (b) is the median of the $RMSE_s$ distribution. 82

3.27 Simulation result of mixture effect in T_2 domain. The black curves represent theoretical signal intensity $\tilde{S}(t)/\tilde{S}_0$, the red curves represent true signal intensity $S(t)/S_0$, and the green curves represent estimated signal intensity $\hat{S}(t)/\hat{S}_0$. The blue dots represent the residuals between $S(t)/S_0$ and $\hat{S}(t)/\hat{S}_0$. The title of each subplot represents the noise level, σ_s, for the current $S(t)/S_0$. 83

3.28 The RSS map of $S(t)/S_0$ and $\hat{S}(t)/\hat{S}_0$. The blue dot represents RSS of initial value, and the pink dot represents RSS of true values ($\alpha = 0.084$ and $\beta = 40$). The white dot represents the minimum RSS, which matches the RSS of the estimates, showing as a black asterisk. 84

3.29 Comparison of true and estimated α and β under abnormal effect in DSC-MR images. The x-axis in each plot represents different noise levels. The red dashed lines in the upper plots indicate the true α and β. 85

3.30 Simulation result of normal effect in DCE-MR domain. The black curves represent theoretical relative signal intensity $\tilde{S}(t)/\tilde{S}_0$, the red curves represent true relative signal intensity $S(t)/S_0$, and the green curves represent estimated relative signal intensity $\hat{S}(t)\hat{S}_0$. The blue dots represent the residuals between $S(t)/S_0$ and $\hat{S}(t)\hat{S}_0$, and the dark grey horizontal lines identify 0. The title of each subplot indicates the noise level, σ_s, increasing from 0.001 to 0.1 with a consistent increment of 0.12. 87

3.31 The RSS image of $S(t)/S_0$ and $\hat{S}(t)/\hat{S}_0$ when $\sigma_5 = 0.051$. The blue dot represents RSS of the initial value of optimisation, and the pink dot represents RSS of true values ($\alpha = 0.18$ and $\beta = 0.5$). The white dot represents the minimum RSS, which matches the RSS of estimation shown as a black asterisk. 88

3.32 Comparison of true and estimated α and β. The x-axis in each plot represents different noise levels. The red dashed lines in the upper plots specify the position of true α and β. 89

3.33 Simulation result of susceptibility effect in DCE-MR domain. The black curves represent theoretical signal intensity $\tilde{S}(t)/\tilde{S}_0$, the red curves represent the true signal intensity $S(t)/S_0$, and the green curves represent estimated signal intensity $\hat{S}(t)/\hat{S}_0$. The blue dots represent the residuals between $S(t)/S_0$ and $\hat{S}(t)/\hat{S}_0$, offset by 1 for improved visualisation, while the dark grey horizontal line marks the reference value of 1. The title of each subplot indicates the noise level, σ_s, which increases from 10^{-4} to 0.01 with a consistent increment of 0.001. 90

3.34 The RSS image of $S(t)/S_0$ and $\hat{S}(t)/\hat{S}_0$ when signal profile is susceptibility and $\sigma_5 = 0.005$. The blue dot represents RSS of initial value, and the pink dot represents RSS of true values ($\alpha = 35.714$ and $\beta = 40$). The white dot represents the minimum RSS, which matches the RSS of estimation shown as a black asterisk. 91

3.35 Comparison of true and estimated α and β. The x-axis in each plot represents different noise levels. The red dashed lines in the upper panels indicate the locations of the true α and β. 92

3.36 Comparison between a motion-free and a motion artifact MR image (Kang et al. 2024). The motion artifact results in blurred, distorted, or ghosted images, which can significantly affect image quality and diagnostic accuracy. 94

4.1 The summary parameters of semi-quantitative approach in DSC-MRI (Paulson et al. 2008; Essock-Burns et al. 2013). 99

4.2 CBV quantification workflow: the pre-processing step (1) addresses CA leakage effects and eliminates recirculation; and step (2) removes dispersion/delay in $C_b(t)$. The step (3a) is the integral ratio method that calculates $rCBV$ as the area under the $C_t(t)$ curve (grey shaded), with $rMTT$ derived from the curve's normalised first moment. The absolute CBV is determined via Equation 4.2. In contrast, the deconvolution method (Step 3b) derives the $R(t)$ from the measurement of blood concentration $C_b(t)$. Absolute MTT is obtained through $R(t)$ integration, absolute CBF is proportional to the peak amplitude f of $R(t)$, and absolute CBV is ultimately determined via the central volume principle (Grøvik et al. 2020). . 104

4.3 Illustration of recirculation effect. The curves are derived from a patient in the ACRIN-6684 dataset, as discussed in chapter 3. . . 106

4.4 An example of the effective residue function $R^{eff}(t)$: The black curve represents both delay and dispersion corrected; the green curve accounts for dispersion correction only; the red curve corrects for delay only; and the blue curve remains uncorrected for both delay and dispersion (Willats et al. 2008). 107

4.5 The summary parameters of semi-quantitative approach in DCE-MRI (F. Khalifa et al. 2014). 111

4.6 Procedure of quantitative analysis: (1) Convert the signal intensity to CA concentration based on the relative signal intensity; (2) Define AIF; (3) Fit model to concentration curve; and (4) estimate the PK parameters (Bernstein et al. 2014). 113

4.7 Schematic illustration of 2C model. The light-grey background represents a tissue, divided into intravascular (blood plasma) and EES compartments. Black dots are CA molecules that passively diffuse across capillary walls into the EES and reverse, driven by concentration gradients. However, CA cannot enter the intracellular space (Bernstein et al. 2014). Notably, the illustrated proportions of plasma volume fraction (v_p) and extracellular volume fraction (v_e) are schematic representations rather than physiologically accurate scales. These proportions remain the same throughout this chapter's schematic illustration. 115

4.8 Schematic illustration of TK model: in the lesion leakage space (dashed box), the CA transfer between intravascular and extracellular space with rate K^{trans} and k_{ep}, respectively (Tofts 2010). . . 117

4.9 ETK model fitting in a normal brain region from DSC-MRI data of an ACRIN-6684 patient. 122

4.10 ETK model fitting in a normal brain region from DCE-MRI data of an ACRIN-6684 patient. 123

5.1 Four ROIs from patient 4221_19. 141

5.2 Workflow of the comparative analysis of the direct optimisation of the ETK model (blue box) and traditional methods (green box). . 142

5.3 Raw relative signal intensities (a) and the traditional method reconstructed concentrations with their estimations using the ETK model (b) in four ROIs from patient 4221_19. 143

5.4 Comparison of reconstructed relative signal intensities for the patient 4221_19 across four ROIs in DSC-MR images. In the upper panel, the red curves represent the raw relative signal $S(t)/S_0$, while the green and blue curves correspond to the reconstructed signals via the conventional method ($(\hat{S}(t)/\hat{S}_0)_A$) and the direct optimisation of the ETK model ($(\hat{S}(t)/\hat{S}_0)_B$), respectively. The lower panel presents boxplots of the residual distributions. The green boxplots show the residuals between $S(t)/S_0$ and $(\hat{S}(t)/\hat{S}_0)_A$, while the blue boxplots represent the residuals between $S(t)/S_0$ and $(\hat{S}(t)/\hat{S}_0)_B$. The red dashed lines indicate the zero-reference level. 145

5.5 Comparison of RMSE deviations between the traditional and direct optimisation methods across all patients in DSC-MRI. The red dashed line indicates the zero-reference level. The table below presents p-values from the paired t-test and the Wilcoxon rank test; values in bold indicate statistical significance ($p < 0.05$). 147

5.6 Deviation of the estimated conversion parameters, $\hat{\alpha}$ and $\hat{\beta}$, between two methods across different anatomical regions. The red dashed line indicates the zero-reference level. The tables embedded in each subplot display p-values from the paired t-test and the Wilcoxon rank test; values in bold indicate statistical significance ($p < 0.05$). 150

5.7 Deviation of the estimated perfusion parameter $\hat{MTT}$ between two methods across different anatomical regions. The red dashed line indicates the zero-reference level. The tables embedded display p-values from the paired t-test and the Wilcoxon rank test; values in bold indicate statistical significance ($p < 0.05$). 151

5.8 Deviation of the estimated perfusion parameters, $\hat{CBV}$ and $\hat{CBF}$, between two methods across different anatomical regions. The red dashed line indicates the zero-reference level. The tables embedded in each subplot display p-values from the paired t-test and the Wilcoxon rank test; values in bold indicate statistical significance ($p < 0.05$). 153

5.9 Raw relative signal intensities (a) and the traditional method reconstructed concentrations with their estimations using the ETK model (b) in four ROIs from patient 4221_19. 154

5.10 Comparison of reconstructed relative signal intensities for the patient 4221_19 across four ROIs in DCE-MR images. In the upper panel, the red curves represent the raw relative signal $S(t)/S_0$, while the green and blue curves correspond to the reconstructed signals via the conventional method ($(\hat{S}(t)/\hat{S}_0)_A$) and the proposed method ($(\hat{S}(t)/\hat{S}_0)_B$), respectively. The lower panel presents boxplots of the residual distributions. The green boxplots show the residuals between $S(t)/S_0$ and $(\hat{S}(t)/\hat{S}_0)_A$, while the blue boxplots represent the residuals between $S(t)/S_0$ and $(\hat{S}(t)/\hat{S}_0)_B$. The red dashed lines indicate the zero-reference level. 155

5.11 Comparison of RMSE deviations between the traditional and proposed methods across all patients in DCE-MRI. The red dashed line indicates the zero-reference level. The table below presents p-values from the paired t-test and the Wilcoxon rank test; values in bold indicate statistical significance ($p < 0.05$). 157

5.12 Deviation of the estimated conversion parameters, $\hat{\alpha}$ and $\hat{\beta}$, between two methods across different anatomical regions. The red dashed line indicates the zero-reference level. The tables embedded in each subplot display p-values from the paired t-test and the Wilcoxon rank test; values in bold indicate statistical significance ($p < 0.05$). 159

5.13 Deviation of the estimated perfusion parameter $\hat{v_p}$ between two methods across different anatomical regions. The red dashed line indicates the zero-reference level. The tables embedded display p-values from the paired t-test and the Wilcoxon rank test; values in bold indicate statistical significance ($p < 0.05$). 160

5.14 Deviation of the estimated perfusion parameters, $\hat{K}^{trans}$ and $\hat{k}_{ep}$, between two methods across different anatomical regions. The red dashed line indicates the zero-reference level. The tables embedded in each subplot display p-values from the paired t-test and the Wilcoxon rank test; values in bold indicate statistical significance ($p < 0.05$). 162

List of Tables

2.1 Summary of exogenous CA-based MR perfusion techniques (Jahng et al. 2014). 31

3.1 The relaxivity values r_2 (unit:$s^{-1}mM^{-1}$) at 37°C (Rohrer et al. 2005). 37

3.2 The mean of relaxivity r_1 (unit:$s^{-1}mM^{-1}$) at 37°C (Rohrer et al. 2005; Noebauer-Huhmann et al. 2010; Shen et al. 2015). 40

3.3 DSC-MRI Profile Consensus. 48

3.4 Three representative signal profiles in DSC-MRI. 49

3.5 DCE-MRI Profile Consensus. 56

3.6 Three representative signal profiles in DCE-MRI. 57

3.7 Simulation value for α in DSC-MRI. 77

3.8 Simulation values for β in DSC-MRI (unit: mmol/L). 77

3.9 Simulation values for α in DCE-MR images. 86

4.1 The summary parameters for semi-quantitative in DSC-MRI. . . . 100

4.2 Quantitative DSC-MRI parameters. 110

4.3 The summary parameters for semi-quantitative in DCE-MRI. . . . 111

4.4 Quantitative DCE-MRI parameters. 126

5.1 Summary of institutions. 138

5.2 Summary of MRI acquisition parameters. 140

I, Yuankun Hu, certify that the work I am submitting is my own and has not been submitted for another degree, either at University College Cork or elsewhere. All external references and sources are clearly acknowledged and identified within the contents. I have read and understood the regulations of University College Cork concerning plagiarism and intellectual property.



Yuankun Hu

Acknowledgements

I would like to take this opportunity to express my sincere gratitude to all those who have supported me throughout my PhD journey.

First and foremost, I am deeply grateful to my supervisors, Prof. Finbarr O'Sullivan and Dr. Jian Huang, for giving me the opportunity to explore this fascinating project. I would like to thank Prof. O'Sullivan for his uniquely creative thinking, enthusiasm for research, invaluable guidance, and unwavering patience, which have greatly contributed to the progress of my research. I would also like to express my sincere appreciation to Dr. Huang for his inspiration during the early stages of the project and for his continued faith and support throughout the years. I am equally thankful to Dr. Eric Wolsztynski for his professional assistance and insightful suggestions, and to Dr. Mark Muzi from the University of Washington for providing the multi-centre clinical dataset and offering valuable advice regarding the data. It has been an honour and a privilege to collaborate with you all.

I would like to extend my thanks to the members of my thesis committee, includ-

ing Prof. Wei Huang from Oakland University, as well as Dr. Supratik Roy, for their constructive feedback and valuable suggestions during the review process. Furthermore, I am sincerely thankful to Dr. Vipin Arora for offering me the opportunity to undertake an internship at Eli Lilly and Company, and to my mentors during that time, Mr. Marcus Ngantcha and Dr. Georgia Martimianaki, whose guidance helped me gain a deeper understanding of how statistical techniques can be applied to make a meaningful impact in real-world settings.

Throughout this PhD journey, I have also received great support from my peers: Dr. Zhaoyan Xiu, Dr. Fengyun Gu, Dr. Qi Wu, Dr. Ran Ren, Xiangyu Meng, and Tao Lan, thank you for the camaraderie, encouragement, and shared moments. Last but not least, I owe my deepest thanks to my parents, my boyfriend, my friends, and my cats. Your constant support, love, and belief in me have been the foundation that enabled me to reach this point. While this thesis represents my individual effort, it stands firmly on the shoulders of the many researchers, mentors, and supporters who have paved the way.

Abstract

Magnetic Resonance Imaging (MRI) is a non-invasive technique that has become an essential tool in diagnosing and staging a wide range of acute and chronic illnesses, including brain cancer. Motivated by a publicly available ACRIN-6684 dataset from an MRI brain tumour imaging study, this thesis investigates alternative approaches for analysing Dynamic Susceptibility Contrast (DSC) and Dynamic Contrast Enhanced (DCE) data, to recover local perfusion and retention characteristics of the administered paramagnetic contrast agent. This approach, named as direct optimisation of the extended Tofts and Kermode (ETK) model, enables effective conversion of MR signal intensity to contrast agent concentration across various anatomical tissues, while mitigating associated artifacts. The direct optimisation of the ETK model method is based on optimisation frameworks that eliminate the need for pre-scan quantification. It simultaneously estimates the contrast agent concentration, the baseline longitudinal relaxation time constant, and relevant perfusion parameters.

The unique recovery of parameters in the proposed method is established through identifiability analysis, and its performance is validated through both numerical

simulations and application to real clinical datasets. Additionally, the root mean square error (RMSE) of the reconstructed signal intensity using the direct optimisation of the ETK model is consistently lower than that achieved by traditional conversion techniques, suggesting improved accuracy and robustness. The variations in signal reconstruction may contribute to discrepancies in the estimation of perfusion parameters across both DSC and DCE imaging protocols. As a result, the enhanced accuracy provided by the direct optimisation of the ETK model has the potential to yield more reliable concentration estimation and, consequently, more accurate perfusion quantification.

Chapter 1

Overview of Thesis

1.1 Introduction

Medical imaging, a transformative technological paradigm in modern healthcare, encompasses a spectrum of minimally invasive modalities, including X-rays, computed tomography (CT), magnetic resonance imaging (MRI), and positron emission tomography (PET), to visualise internal anatomical structures and physiological processes. These imaging techniques facilitate accurate disease diagnosis, guide therapeutic strategy formulation, and enable longitudinal monitoring of pathological progression. Unlike CT and PET, which involve exposure to ionising radiation, MRI employs radiofrequency (RF) pulses within static magnetic fields, thereby eliminating carcinogenic risks associated with photon exposure.

MRI technique, including structural MRI and perfusion MRI, has become an indispensable tool for delineating neuroanatomical architecture and assessing a wide range of central nervous system (CNS) pathologies. Perfusion MRI methodologies, through quantitative analysis of contrast agent (CA) kinetics based on the MRI signal, enable functional characterisation of tissue hemodynamics, significantly improving diagnostic precision in CNS disorders while supporting more informed therapeutic decision-making and longitudinal assessment of treatment efficacy (Essig et al. 2013). These kinetic analyses, however, rely heavily on the accurate estimation of CA concentration, since the relationship between signal intensity and CA concentration is nonlinear in most cases. MRI measures the effect of CA on proton relaxation times, rather than directly capturing signal changes resulting from CA uptake, making precise concentration mapping essential for reliable kinetic modelling (Gadian et al. 1985; F. Khalifa et al. 2014).

This thesis focuses on improving the accuracy of signal reconstruction and the corresponding concentration estimation, as well as enhancing the reliability of perfusion parameter estimations in both dynamic susceptibility contrast (DSC) and dynamic contrast enhanced (DCE) MRI techniques. We first evaluate existing signal conversion techniques and subsequently propose a novel signal reconstruction algorithm, a two-parameter method, designed to address limitations inherent in conventional approaches. The identifiability analysis and numerical simulations have proven the feasibility, robustness, and accuracy of the proposed method. Using a retrospective clinical dataset, we demonstrate that the two-parameter model, nested within the extended Tofts and Kermode (ETK) model and referred to as the direct optimisation of the ETK model, offers improved computational

efficiency and enhanced parameter quantification accuracy. Variations in perfusion parameter estimates indicate that signal reconstruction accuracy significantly influences the estimation of physiological and pathological characteristics.

1.2 Main Contributions

The principal contributions of this thesis are summarised as follows:

A novel **two-parameter technique** is proposed to convert the relative MR signal intensity time course, $S(t)/S_0$, where $S(t)$ and S_0 denote the dynamic and baseline signal intensities, respectively, into the corresponding tissue CA concentration time course, $C_t(t)$, by incorporating the associated baseline relaxation time, T_{10}. The unique recovery of parameters is established, and supporting numerical simulations confirm its reliability and stability under varying conditions. Further validation using clinical data incorporates the ETK model to estimate $C_t(t)$, referred to as the **direct optimisation of the ETK model**, thereby imposing physiologically reasonable constraints on the reconstructed concentration. This integration ensures that the reconstruction remains consistent with known tissue perfusion characteristics. Overall, the proposed direct optimisation of the ETK model approach proves effective in both signal reconstruction and perfusion parameter estimation across DSC- and DCE-MRI.

In addition, we present **an overview of existing signal conversion methodologies,** including the pre-contrast inversion recovery (IR) technique, the Look-Locker

(LL) technique, and the multiple flip angle (MFA) technique, highlighting their theoretical underpinnings and practical limitations.

Furthermore, we also present **a review of pharmacokinetic modelling approaches for quantitative DSC- and DCE-MRI analysis**. For DSC-MRI, the review outlines correction strategies developed to address violations of modelling assumptions. For DCE-MRI, the review focuses on compartmental modelling frameworks, with particular emphasis on the Tofts model and its extended version. We also summarise the common objective of quantitative analysis in both DSC- and DCE-MRI, emphasising that once the concentration is obtained, the compartmental models can be applied regardless of the imaging protocol.

1.3 Thesis Structure

This thesis comprises six chapters. The structure of each chapter is as follows: chapter 2 begins with a brief discussion of various medical imaging modalities and provides an overview of recent developments in MR scanner technologies. It introduces the fundamental imaging mechanisms and key parameters in MRI, followed by a description of the spoiled-GRE sequence. The chapter also introduces the spoiled-GRE equation with perfusion MR imaging and discusses the application of contrast agents. Finally, it outlines the advantages of MRI alongside its associated risks.

Additionally, chapter 3 reviews existing approaches for converting MR signal

intensity to CA concentration and evaluates common artifacts encountered during MR signal reconstruction. Building on these insights, this chapter proposes a novel two-parameter method designed to enhance the robustness and physiological relevance of signal conversion. The method is validated through theoretical identifiability analysis and comprehensive numerical simulations under varying noise conditions. Subsequently, chapter 4 presents a review of pharmacokinetic modelling techniques used in DSC- and DCE-MRI, highlighting their respective assumptions, advantages, and limitations. This review provides the conceptual foundation for model integration in subsequent analyses. Finally, chapter 5 applies the proposed direct optimisation of the ETK model to clinical datasets. The performance of the direct optimisation of the ETK model is evaluated against conventional methods for reconstructing relative signal intensity curves and estimating perfusion parameters across multiple brain regions. Results show that the proposed method provides improved accuracy and physiological consistency across diverse anatomical tissues.

In chapter 6, the thesis is summarised by highlighting its key findings and methodological contributions. This chapter also discusses potential clinical applications of the proposed approach and outlines directions for future research, with an emphasis on translational opportunities and technical refinements.

Chapter 2

Background of MRI

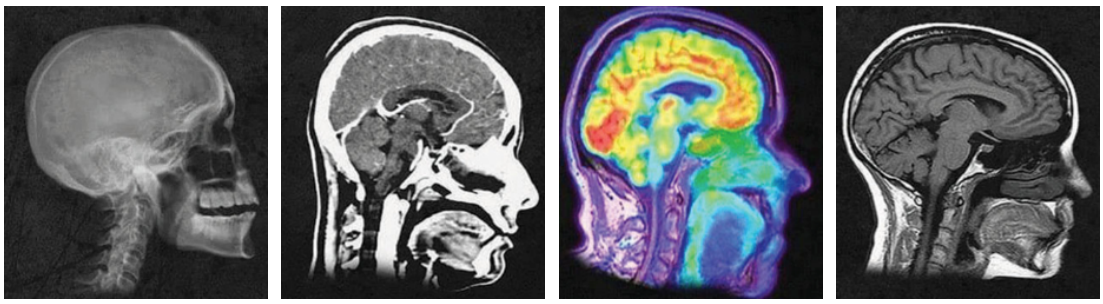
Medical imaging is a modern, non-invasive technology that enables the assessment of the morphological, physiological, and pathological conditions of human tissues and organs through physical measurement techniques. This chapter begins with a brief overview of several commonly used medical imaging modalities, followed by a detailed introduction to magnetic resonance imaging (MRI), which is the primary focus of this thesis. It discusses the technological developments and fundamental principles of MRI, along with the spoiled gradient recall echo (spoiled-GRE) sequence and equation. Special attention is given to perfusion MRI based on spoiled-GRE sequences, such as DSC- and DCE-MRI, with emphasis on the role of contrast agents. The chapter concludes by outlining the advantages and limitations of MRI, as well as the potential benefits of integrating multiple imaging modalities in clinical practice.

2.1 Medical Imaging

Medical imaging techniques, such as ultrasound and CT, refer to the methods and procedures used to generate non-invasive visual representations of the body's internal structures. These methods play a critical role in diagnosing medical conditions and guiding interventions, as well as evaluating the functionality of specific organs or tissues. The origins of medical imaging can be traced back to 1895, when Wilhelm Conrad Roentgen discovered X-rays (Bercovich et al. 2018). In an X-ray imaging process, a tube emits high-energy electromagnetic radiation that penetrates the body, with varying absorption rates depending on the density and composition of the tissues. Specifically, the dense tissues like bones absorb more X-rays, resulting in fewer X-rays reaching the detector and appearing white in the final image. Conversely, the soft tissues, such as muscles and organs, are less dense and allow more X-rays to pass through, displaying various shades of grey. In the air-filled regions, such as the lungs, absorb minimal X-rays. Thus, these areas appear darker or black on the X-ray image (Ou et al. 2021).

X-ray technologies can be further enhanced to capture higher spatial and temporal resolutions. For instance, CT technology, developed by Hounsfield and Cormack in the 1970s, provides detailed three-dimensional (3D) views of soft tissues and bones. The CT scanners utilise rotating X-rays combined with advanced computer algorithms to generate cross-sectional images of the body. In addition, the CT perfusion imaging, involving the injection of contrast agents, is employed to evaluate blood flow through vessels (Wittsack et al. 2008). In the following decade, nuclear medicine imaging techniques, such as single photon emission computed

tomography (SPECT) and positron emission tomography (PET), were introduced into clinical practice. These modalities rely on the administration of targeted radioactive pharmaceuticals, which provide functional insights into physiological processes. However, during the same period, MRI, a technique that does not involve ionising radiation, gained widespread use. MRI leverages magnetic fields and radio waves to produce high-resolution images of soft tissues, making it a preferred modality for achieving superior spatial resolution and physiological data. Furthermore, functional MRI (fMRI), introduced in the 1990s, allows for the visualisation of brain activity by detecting changes in blood flow, thereby expanding MRI's utility in both clinical and research applications. Figure 2.1 presents four sagittal view medical images of the human brain, each acquired using a different imaging technique.



(a) X-Ray (b) CT (c) PET (d) MRI

Figure 2.1: The sagittal brain images from X-Ray, CT, PET, and MRI (Kshatri et al. 2023).

While MRI is the primary focus of this thesis, it is not used in isolation. Over the past two decades, the development of hybrid imaging systems, such as PET-MR, has significantly advanced diagnostic capabilities. These technologies offer more precise and comprehensive insights, particularly in the context of cancer diagnosis and treatment (Jadvar et al. 2014).

2.2 Magnetic Resonance Imaging

MRI is a non-invasive imaging modality that delivers exceptional anatomical and physiological or functional information without the use of X-rays or radioactive tracers. MR scanners employ strong magnetic fields, typically ranging from 1.5 Tesla to 3 Tesla, and radiofrequency (RF) waves to generate high-resolution images of internal organs and tissues, with particular efficacy in imaging soft tissues such as the brain and abdomen. This section will outline the development of MRI technology and explain its underlying mechanisms.

2.2.1 Development of MR Scanners

The development of MRI can be traced back to the early twentieth century, with significant contributions from physicists, chemists, biologists, and mathematicians/statisticians who were instrumental in the discovery of nuclear magnetic resonance (NMR) and established the foundational principles of MRI. The initial discovery of NMR by Isidor Isaac Rabi in 1944 provided the theoretical groundwork for MRI technology (Rinck 2019). Subsequently, in 1946, Felix Bloch advanced the field by publishing a mathematical analysis of the "nuclear induction" phenomenon, presenting a set of equations that explain the origin and characteristics of the NMR signal (Bloch et al. 1946).

1950-1960s: Pioneering Ideas for MRI. In the 1950s, significant advancements in MRI technology began with Erwin Hahn's groundbreaking detection of spin

echoes and free induction decay (Hahn 1950a; Hahn 1950b). Following this, in 1953, Herman Carr developed the first one-dimensional (1D) NMR spectrum (Carr 1953). In addition, notable early work on relaxation time measurement was published in 1955 by Erik Odeblad and Gunnar Lindström, a physician and a scientist from Stockholm, who investigated living cells and excised animal tissues. Their work is recognised as a pioneering contribution to the discovery and development of MRI (Rinck 2019; Odeblad et al. 1955).

1960-1970s: From Spectra to Imaging. During this period, Vladislav Ivanov advanced the field by employing magnetic field gradients in conjunction with selective frequency excitation and readout techniques to encode spatial coordinates (MacWilliams 2003). In 1969, Dr. Raymond Damadian made a significant breakthrough by demonstrating that magnetic resonance could differentiate between cancerous and non-cancerous cells in rats. This work marked a pivotal milestone in the application of NMR to medical imaging and led Damadian to propose the development of an MR body scanner (Damadian 1971).

1970-1980s: The first clinical MRI scanner. Starting in 1972, chemist Paul C. Lauterbur made significant contributions by reconstructing two-dimensional (2D) images through the use of magnetic field gradients, subsequently stacking these images to form 3D representations (Lauterbur 1973). In the late 1970s, Peter Mansfield further advanced MR imaging techniques by refining methods for image acquisition and processing. These developments culminated in the installation of the first 1.5 Tesla clinical MRI scanners in the early 1980s (Mansfield 1977).

1980-1990s: Advancements in MRI Technology and Contrast Agents. This era witnessed some substantial improvements in MRI resolution and imaging techniques. Clinically, 1.5 Tesla whole-body systems began to be commercially available starting in the mid-1980s. Subsequently, major MRI manufacturers explored the potential of higher field systems, with a limited number of 4 Tesla systems being investigated in the late 1980s due to their superior signal-to-noise (SNR) ratio (Martin John Graves 2022). In 1988, the introduction of the first gadolinium-based contrast agent (CA), gadopentetate dimeglumine (Magnevist), was available for clinical use. These agents improved the ability to highlight and differentiate various tissues, enhancing the diagnostic capabilities of MRI (Lohrke et al. 2016).

1990s-2000: Functional Magnetic Resonance Imaging (fMRI). In 1993, the University of Nottingham and Oxford Instruments collaboratively developed a 3 Tesla MRI system, which was subsequently approved by the FDA (U.S. Food and Drug Administration) for commercial clinical use between 1999 and 2002 (Martin John Graves 2022). Among the most significant innovations in MRI during this period were the advent of ultra-high-field MRI systems and high-density phased array coils. These advancements markedly improved the SNR ratio and facilitated the development of advanced imaging applications (Uematsu et al. 2004; Fukatsu 2003). Additionally, a landmark discovery by Ogawa in 1990 demonstrated that changes in blood oxygenation levels could be measured using MRI, laying the foundation for a new era of functional imaging (Ogawa et al. 1990). This advancement enabled the detailed visualisation of brain activity and has since driven substantial developments in fMRI, broadening its application in

both research and clinical settings.

2000-Present: Recent Advances in MRI Technology. From the 2000s to nowadays, MRI has witnessed continuous evolution, marked by several significant innovations. One of the major advancements has been the development and implementation of ultra-high-field MRI systems, such as the 7 Tesla MRI scanner (Kabasawa 2022), with the Magnetom Terra.X from Siemens Healthineers® receiving FDA approval in 2017[1]. Even higher field strengths, such as the 10.5 Tesla MRI scanners, have been developed for research purposes, pushing the boundaries of imaging resolution and diagnostic potential (Grant et al. 2020). Furthermore, the integration of artificial intelligence (AI) and machine learning algorithms into MRI technology has revolutionised image acquisition, analysis, and interpretation, allowing for more efficient and accurate diagnostic processes (M. Khalifa et al. 2024).

2.2.2 Mechanism of MRI

MRI operates by utilising strong magnetic fields to manipulate and measure the magnetic properties of atomic nuclei, primarily hydrogen nuclei (protons), which constitute approximately 70% of the human body. These protons resonate at a specific frequency known as the Larmor frequency (ω_0) (Larmor 1897; Tubridy et al. 2000). During the imaging process, the MRI scanner generates a strong homogeneous static magnetic field, denoted as B_0, which is proportional to the

[1] `https://www.fda.gov/news-events/press-announcements/fda-clears-first-7t-magnetic-resonance-imaging-device`

Larmor frequency ($\omega_0 = \gamma * B_0$, with γ representing the gyromagnetic ratio of the proton, approximately 42.58MHz/T). This magnetic field causes the hydrogen protons in water and fat molecules within the body to align with the field, typically along the longitudinal axis of the MRI scanner, as illustrated in Figure 2.2. The RF waves, commonly referred to as B_1 and perpendicular to B_0, are generated by driving electrical currents to excite the nuclei.

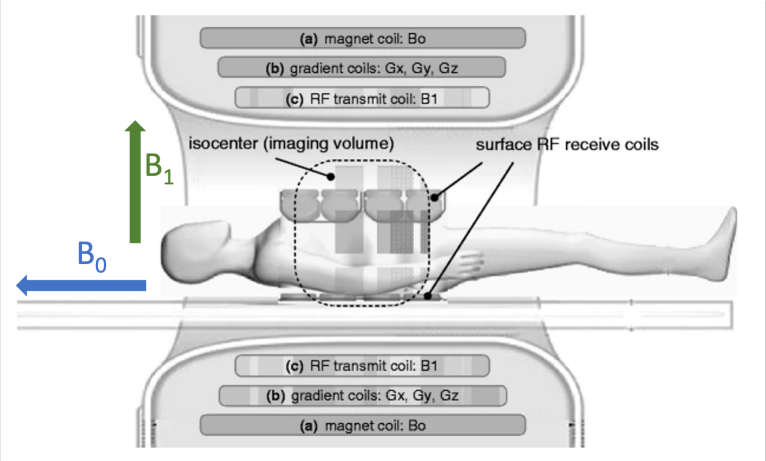


Figure 2.2: Scheme of MRI: (a) magnet coil to produce B_0; (b) gradient coil to produce time-varying gradient fields; (c) RF coil to generate B_1 (Moser et al. 2009).

When the nuclei are exposed to a specific RF frequency, they absorb energy and transition to a higher energy state. The magnetic field strength can be electronically modulated along the body using gradient coils, allowing small adjustments to the local magnetic field. This results in different slices of the body resonating at distinct frequencies as they are selectively targeted. Once the RF pulse is switched off, the nuclei release the absorbed energy as they gradually return to their lower energy state, a process known as relaxation. The emitted energy during relaxation is detected and used to create the MR images (Creager

et al. 2012). Sequential RF pulses can be applied to enhance the visibility of specific tissues or detect abnormalities, as the relaxation rates vary across tissue types after the RF pulse ceases. Figure 2.3 demonstrates a procedure of two magnetic fields (B_0 and B_1) applied in MR. These illustrative MRI mechanism images are adapted from materials provided by the University of Florida's MRI resource page[2].

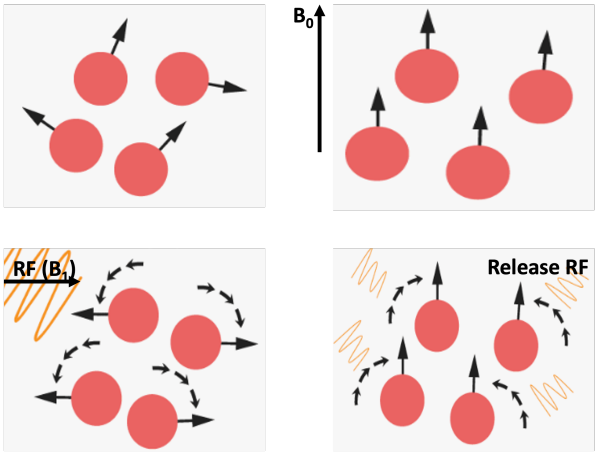


Figure 2.3: The mechanism of MRI: the picture in the top left presents protons that are randomly oriented in the body without a magnetic field. When a magnetic field is applied, most of the protons align with the direction of the magnetic field B_0, as seen in the top right. Once an RF is emitted, the protons tilt sideways (bottom left) and they return to their original alignment as the RF is turned off (bottom right).

During this procedure, proton relaxation is quantified in two ways: first, by measuring the time it takes for the longitudinal magnetisation of the spins to return to alignment with the main magnetic field B_0, known as the T_1 relaxation time (unit: millisecond (ms)); second, by measuring the time required for the axial spin to realign, referred to as T_2 relaxation time (unit: ms) (Bloch et al. 1946; Berger 2002).

[2] `https://merritt.biochem.med.ufl.edu/about-mri/`

2.2.2.1 Time Parameters of MRI

A critical aspect of MRI is the use of time-related parameters that govern image contrast and signal behaviour. In addition to the intrinsic T_1 and T_2 relaxation times of tissue protons, acquisition parameters within pulse sequences, such as repetition time (TR) and echo time (TE), also play essential roles in determining tissue appearance on MRI scans. These parameters are fundamental in differentiating between various tissue types and detecting abnormalities, as they directly affect signal intensity and contrast in the final image.

T_1 relaxation time: The T_1 relaxation time, also known as the longitudinal or spin-lattice relaxation time, represents the period required for the net magnetization to return to its equilibrium state following the excitation pulse. The recovery of longitudinal magnetization, denoted as M_z, is described by an exponential function:

$$M_z(t) = m_0 * (1 - exp(-\frac{t}{T_1})) \tag{2.1}$$

where M_z is the longitudinal component of net magnetisation M. The m_0 is the equilibrium magnetisation, and T_1 is the time constant characterising this process. The T_1 value represents the time it takes for the magnetisation to recover approximately 63% $(1 - 1/e)$ of its equilibrium value (John P Ridgway 2010). Figure 2.4 illustrates this regrowth process.

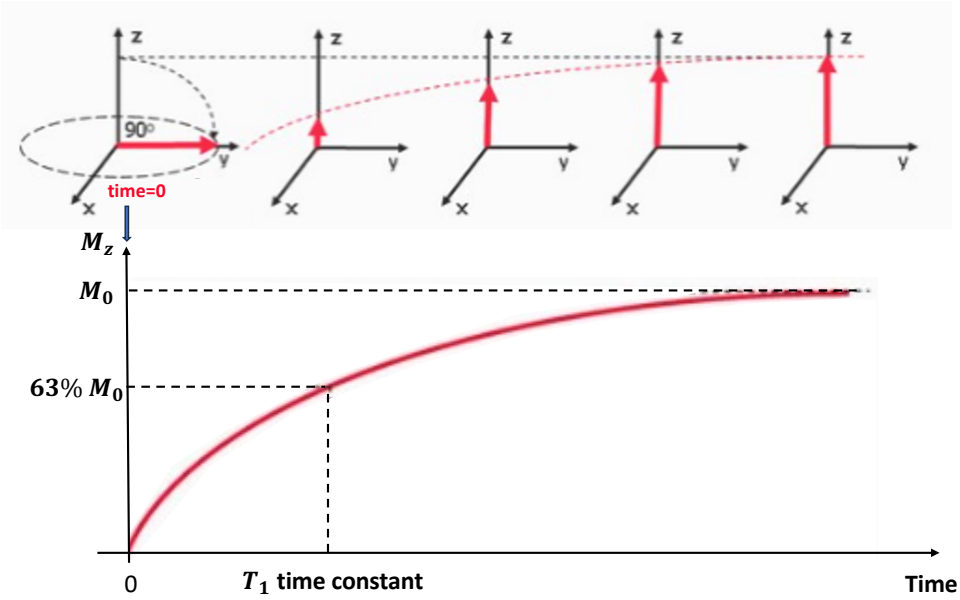


Figure 2.4: The T_1 relaxation time: an exponential recovery of longitudinal magnetization (M_z) following the application of a 90° RF pulse at equilibrium. After excitation, M_z gradually returns toward its baseline value (Tadanki 2018).

T_2 relaxation time and T_2^*: The T_2 relaxation time, also known as the transverse or spin-spin relaxation time, represents the decay of magnetization within the transverse plane back to its equilibrium value of zero. The formula below describes an exponential decay of T_2:

$$M_{xy}(t) = m_0 * exp(-\frac{t}{T_2}) \tag{2.2}$$

where M_{xy} is the transverse component of net magnetization M and T_2 is the time constant characterising this process. In practice, however, the apparent transverse relaxation time, denoted as T_2^*, is shorter than the theoretical T_2 due to

inhomogeneities in the main magnetic field (B_0). Consequently, T_2^* is always less than or equal to T_2, leading to the "observed" or "effective" transverse relaxation time, i.e., $T_2^* \leq T_2 < T_1$ (Chavhan et al. 2009). This process of signal attenuation is known as free induction decay (FID), which characterises the exponential reduction of transverse magnetisation to approximately 37% ($1/e$) of its initial value following a 90° RF pulse. Figure 2.5 illustrates this procedure.

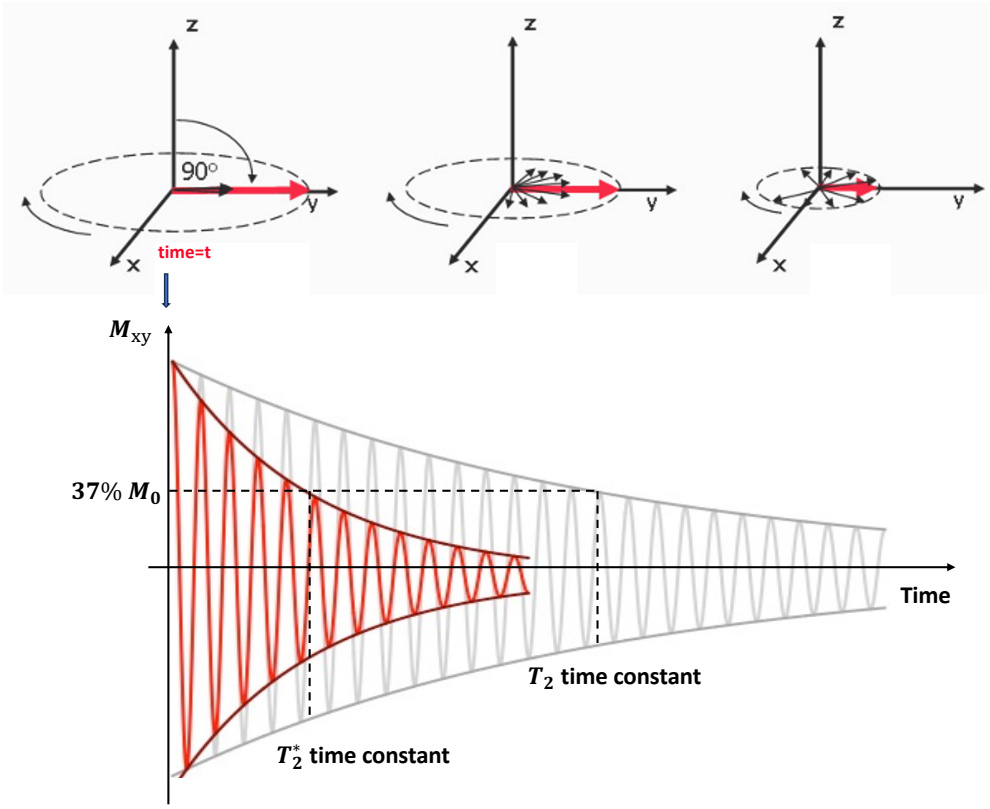


Figure 2.5: The T_2 and T_2^* relaxation time: following the application of a 90° RF pulse at time t, transverse magnetisation undergoes exponential decay. The dark grey curve represents the T_2 relaxation, while the dark red curve represents the more rapid T_2^* decay, known as FID (Chavhan et al. 2009).

Echo time (TE): A single 90° RF pulse generates a FID signal, whereas two successive RF pulses, the first is 90° followed by a 180° pulse, produce a spin echo

(SE). The time interval between the centre of the initial RF pulse and the peak of the SE is defined as the TE (Hahn 1950b). This parameter, measured in ms, plays a crucial role in influencing the extent of transverse relaxation (Gold et al. 2004). In pulse sequences designed to generate multiple echoes following each RF pulse, various echo times can be defined, typically denoted as TE_1, TE_2, TE_3, and so forth (Hendrick et al. 2005). Figure 2.6 elucidates this concept.

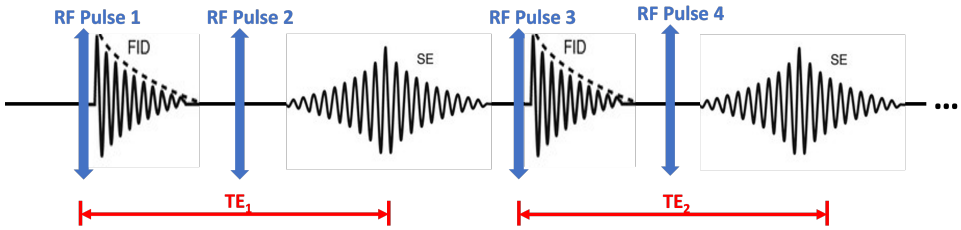


Figure 2.6: The multiple echoes produced by RF pulse sequences (Chow et al. 2022).

Repetition time (TR): Typically measured in ms, it refers to the interval from the start of one pulse sequence, including the RF excitation pulse, to the start of the subsequent repetition of the same sequence. This interval dictates the degree of longitudinal relaxation that can occur before the next excitation. Figure 2.7 illustrates a relationship between MR signal intensity and these time parameters.

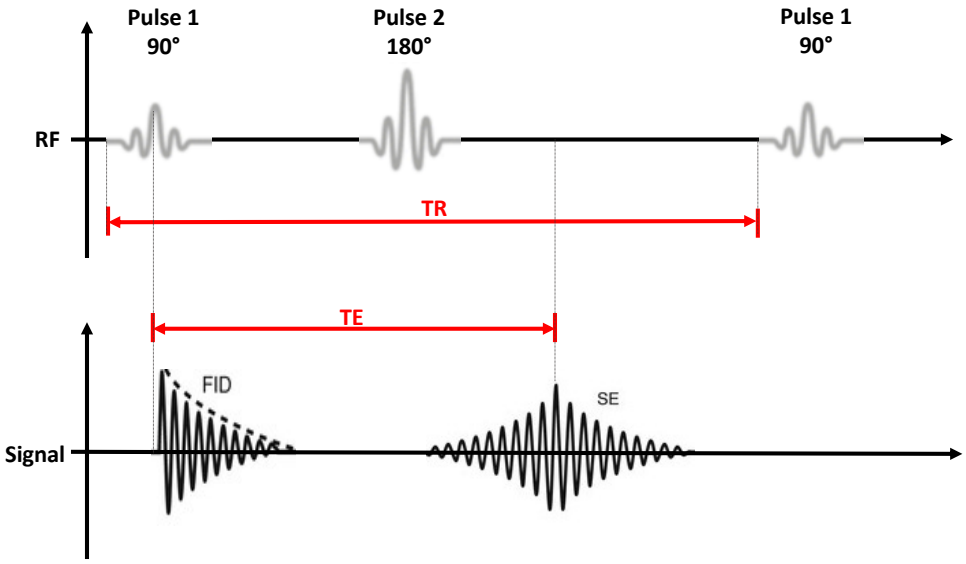


Figure 2.7: Relationship between MR signal intensity, RF, TE, and TR (Shamir et al. 2025).

2.2.2.2 Gradient Echo and Spoiled Gradient Echo Sequences

MR sequences consist of specific combinations of RF pulses and gradient fields designed to manipulate the magnetic properties of protons, thereby generating images with particular contrast characteristics. Each sequence differs in timing, RF pulse, and imaging parameters, enabling the acquisition of distinct types of anatomical and physiological information. Among these, the spoiled-GRE sequence is a specific type of gradient echo (GRE) sequence designed to eliminate residual transverse magnetisation through spoiling mechanisms.

The GRE sequence, which uses a single RF pulse with a gradient reversal, is commonly termed GRE in Siemens® and General Electric Healthcare® systems. GRE sequences differ from conventional MRI sequences in two key aspects: (1)

they utilise gradient reversal to generate the echo in the transverse plane; and (2) the flip angle (FA), denoted as θ, is often less than 90° (John P. Ridgway 2015). The FA refers to the amount of rotation the net magnetization M experiences during application of an RF pulse. In GRE sequences, the FA commonly varies within a range of 10° to 80° . The GRE is generated by the frequency-encoded gradient, which is applied twice in succession but in opposite directions. Initially, the gradient is applied in reverse to induce transverse dephasing of the spinning protons. Afterward, it is used as a readout gradient to re-align the dephased protons and acquire the signal, as illustrated in Figure 2.8. The GRE sequence makes the acquisition faster, but it also increases sensitivity to magnetic field inhomogeneities, impacting the signal quality and image contrast (Pui et al. 1995; Boyle et al. 2006).

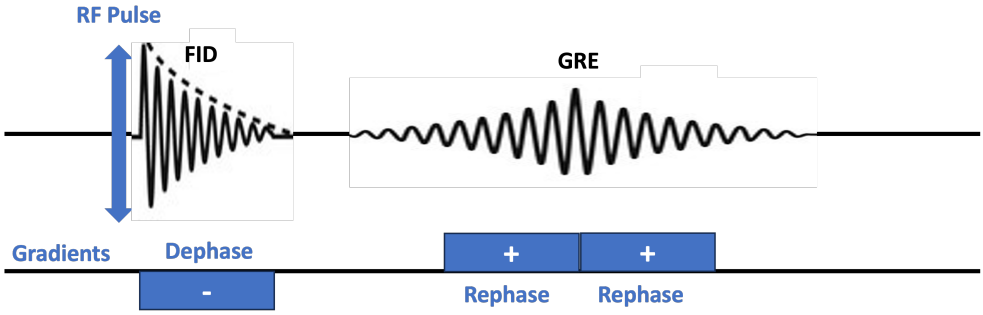


Figure 2.8: Generation procedure of GRE sequences (Selvakumar et al. 2014).

Among various GRE implementations, the spoiled-GRE sequence represents a specific variant. It is commonly referred to as FLASH on Siemens® systems and SPGR on General Electric Healthcare® platforms. The term “spoiled” refers to the elimination of residual transverse magnetisation from previous excitations, achieved through either gradient spoiling or phase cycling (RF spoiling). This

process prevents image artifacts caused by residual coherence from earlier excitations. Spoiled-GRE technique is primarily designed to disrupt transverse coherence, providing high contrast between tissues with different T_1 relaxation times, which is especially useful for DCE studies (Chavhan et al. 2008; Markl et al. 2012). Although the major benefits of spoiled-GRE sequences are producing better T_1-weight image, the T_2^*-weight images, such as DSC-MRI, can be achieved by appropriate selection of parameters (Chavhan et al. 2009). Therefore, spoiled-GRE sequences are widely employed in MRI due to their versatility and ability to acquire images in both 2D and 3D modes, offering rapid image acquisition. Additionally, their flexibility in manipulating contrast parameters makes them essential for imaging nearly every part of the body. This adaptability has led to their ubiquitous use in clinical MRI, allowing for detailed anatomical visualisation and dynamic studies (Hargreaves 2012).

2.2.3 Image Reconstruction

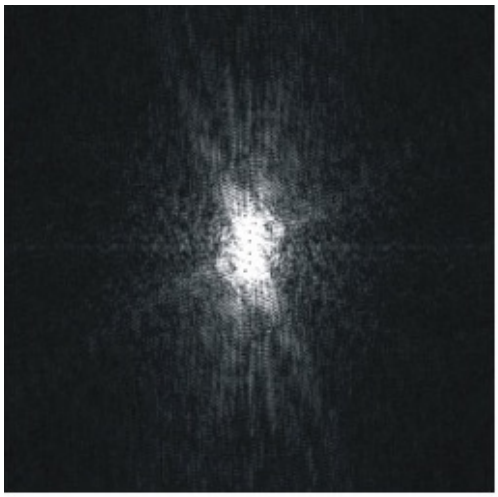
MRI reconstruction refers to the process of converting the raw data acquired during a scanning process into interpretable images. This involves applying mathematical techniques to the signals recorded in k-space, the spatial frequency domain in which MRI data is initially stored. The process then uses advanced mathematical algorithms (such as the Fourier transform) to convert the spatial frequency data into a 3D visualisation of the MRI image (Hansen et al. 2015; Haidekker 2013). The general procedure is illustrated in Figure 2.9.



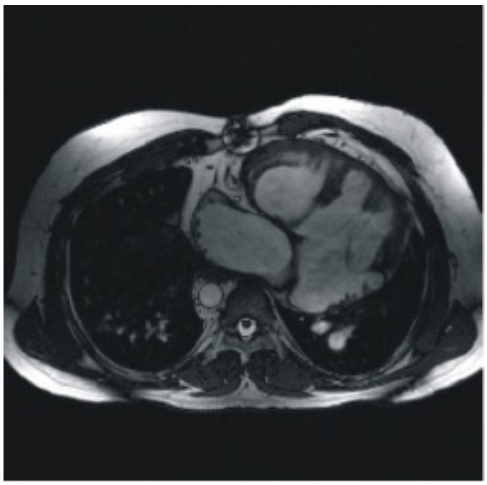
(a) SIEMENS Healthineers® MR scanner.



(b) Digitised MR signal.



(c) k-space (Moratal et al. 2008).



(d) k-space associated image (Moratal et al. 2008).

Figure 2.9: A procedure of MR image reconstruction. MR imaging begins with signal encoding performed by the scanner hardware, which includes RF transmission/reception and spatial gradients. The encoded signals are sampled and mapped into k-space. Finally, a Fourier transform is applied to reconstruct images from the k-space data.

2.2.3.1 k-space

The k-space serves as the initial domain for storing digitised MR signals, typically arranged on a rectangular grid. The axis of k-space are denoted as k_x (horizontal) and k_y (vertical). The horizontal axis, k_x, corresponds to the frequency encoding direction, while the vertical axis, k_y, represents the phase encoding direction of the excited protons. The relationship between k-space and final image is governed by the Fourier transformation (Moratal et al. 2008). The complete image is generated by applying a 2D inverse Fourier transform to the full k-space dataset, thereby integrating all spatial frequency components. The spatial frequencies and orientation of the data vary depending on the location of the pixel within k-space. Conventionally, low spatial frequencies are located near the centre of k-space, while higher spatial frequencies reside toward the periphery. Each point's intensity in k-space indicates its relative contribution to the reconstructed image, for example, brighter points represent greater influence on specific spatial frequency components (Gallagher et al. 2008). It is important to note that individual coordinates (K_x, K_y) in k-space do not correspond directly to specific pixel locations (x, y) in the final image. Rather, each k-space point contains spatial frequency and phase information that collectively contribute to the formation of all image pixels. Figure 2.10 briefly illustrates this relationship.

In practical MR imaging, the method of sampling and manipulating k-space has a major impact on the resulting image. For example, adjusting the field of view (FOV), applying various filters (e.g., low-pass or high-pass), and employing acceleration techniques such as partial Fourier imaging all influence how k-space

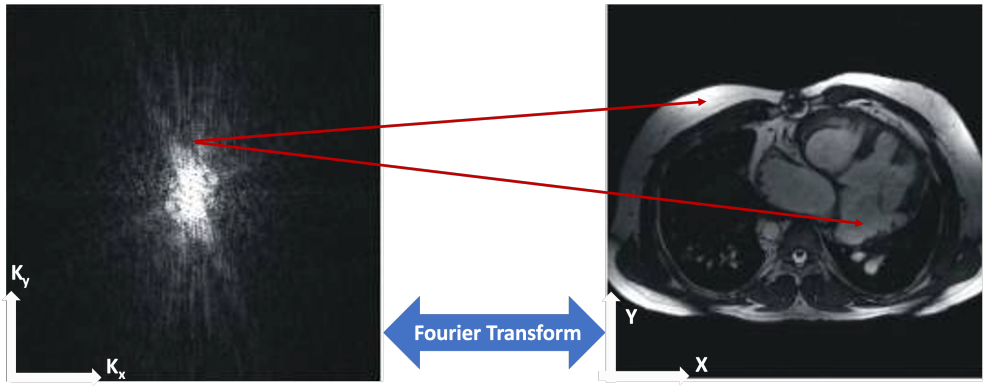


Figure 2.10: k-space (left) and its associated image (right) of a patient with transposition of great vessels. Each point in k-space contributes to the entire image, and conversely, each pixel in the image is influenced by all points in k-space, reflecting their Fourier relationship (Moratal et al. 2008).

is populated. These modifications directly affect the spatial resolution, contrast, and potential artifacts in the final MR image (Moratal et al. 2008; Jornada et al. 2016).

2.2.3.2 DICOM

After transformation, the final MR image is saved in the DICOM (Digital Imaging and Communications in Medicine) format, which has become the standard for storing, transmitting, and sharing medical imaging data. In addition to the image itself, DICOM files embed metadata that document key details of the imaging study, including patient demographics, acquisition parameters (e.g., magnetic field strength, pulse sequence), spatial resolution, and other relevant information (Kahn et al. 2007). The DICOM format ensures that images are systematically organised, stored, and readily shareable across various healthcare systems, facilitating seamless communication between imaging devices and medical

software (Bidgood Jr et al. 1997).

2.3 Spoiled-GRE Equation

Once the dynamic MR images have been acquired, quantitative analysis requires the reconstruction of contrast agent concentration from signal intensity to generate kinetic information, especially in the perfusion images. At the preliminary stage of signal-to-concentration conversion, the spoiled-GRE equation is used to model the relationship between MR signal intensity and tissue relaxation properties. The signal in a spoiled-GRE sequence is governed by four time-fixed parameters: equilibrium magnetisation (m_0), repetition time (TR), echo time (TE), and flip angle (FA, θ), as well as two time-varying relaxation times, $T_1(t)$, $T_2^*(t)$. Assuming that a longitudinal steady state has been achieved and perfect spoiling is accomplished, the signal intensity ($S(t)$) in a spoiled-GRE sequence is expressed as (Buxton et al. 1987):

$$S(t) = m_0 \cdot sin(\theta) \cdot \frac{1 - exp(-\frac{TR}{T_1(t)})}{1 - cos(\theta) \cdot exp(-\frac{TR}{T_1(t)})} \cdot exp(-\frac{TE}{T_2^*(t)}) \tag{2.3}$$

In the concentration reconstruction process, DSC-MRI relies exclusively on the T_2^*-weighted signal contribution, represented by the term $exp(-\frac{TE}{T_2^*(t)})$. In contrast, DCE-MRI focuses solely on the T_1-weighted component, given by

$(1 - exp(-\frac{TR}{T_1(t)}))/(1 - cos(\theta) * exp(-\frac{TR}{T_1(t)}))$. However, neglecting one of the relaxation effects in each protocol can lead to inaccuracies, and reconstructing the MR signal from the converted concentration $C_t(t)$ may introduce noise in both imaging protocols.

2.4 Perfusion MR Imaging

Perfusion is a fundamental biological process and perfusion MRI is particularly sensitive to the microvasculature. It has been employed in a wide range of clinical applications, including tumour grading, stroke localisation, and the characterisation of various other diseases (Jahng et al. 2014). The three primary perfusion techniques used in MR imaging are DSC-MRI, DCE-MRI, and arterial spin labelling (ASL) MRI. Both DSC- and DCE-MRI involve the administration of an exogenous contrast agent (CA) to enhance image contrast and provide detailed information on tissue perfusion and vascular characteristics. In contrast, ASL is a non-contrast technique that uses magnetically labelled inflowing arterial blood water as an endogenous tracer to quantify perfusion (Deibler et al. 2008; Essig et al. 2013).

2.4.1 DSC-MRI

DSC-MRI employs rapid imaging to capture the first pass of a CA bolus, and is therefore also referred to as bolus tracking MRI. The signal changes in DSC-MRI

rely on susceptibility effects, which alter the T_2 or T_2^* signal in the presence of CA. Following intravenous injection, the CA induces local magnetic field inhomogeneities, leading to a reduction in T_2^* signal intensity due to increased magnetic susceptibility (Jahng et al. 2014).

When spoiled-GRE acquisition is used, imaging parameters such as TR, TE are typically set to relatively long values and a moderate flip angle is selected to minimise T_1 contamination (Fernando Calamante et al. 2007). Quantitative perfusion parameters, such as cerebral blood volume (CBV) and cerebral blood flow (CBF), are used to assess cerebral perfusion and vascular properties. This technique is particularly valuable in neuroimaging for evaluating conditions, such as brain tumours, stroke, and other cerebrovascular disorders (Ferré et al. 2012; M. S. Shiroishi et al. 2015).

2.4.2 DCE-MRI

DCE-MRI utilises T_1-weighted contributions to dynamically track CA distribution over time. Following bolus injection, the DCE-MRI signal depends on T_1 relaxation time and increases due to the T_1 shortening effect induced by the paramagnetic CA (Erlemann et al. 1989).

The spoiled-GRE sequence is commonly employed in DCE-MRI. For quantitative DCE-MRI analysis, a pre-contrast mapping of T_1, denoted as T_{10}, is required. During dynamic acquisition, imaging parameters, such as TR, TE, and θ, are

typically set to short values to optimise T_1-weighting and temporal resolution. Pharmacokinetic modelling techniques, such as the Tofts model, are used to obtain perfusion parameters. One such parameter is the transfer constant (K^{trans}), which reflects capillary permeability or blood flow in different physiologic environments. These parameters facilitate the assessment of brain tumours, as well as diseases of the breast, prostate, pelvis, and muscle. The ability of DCE-MRI to provide real-time, functional information on blood flow and capillary permeability makes it a valuable tool in both the diagnosis and monitoring of various pathological conditions (Gordon et al. 2014; Cárdenas-Rodríguez et al. 2016).

2.4.3 ASL-MRI

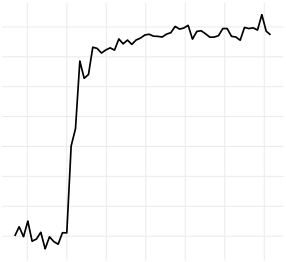
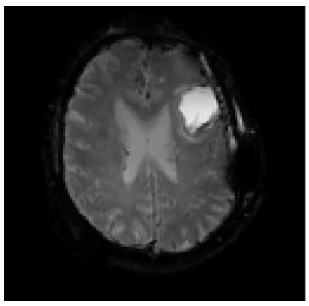
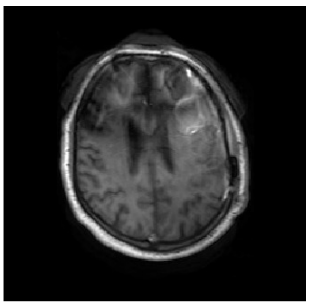
ASL offers a completely non-invasive alternative to contrast-based perfusion MRI methods, as it does not involve the use of injected CAs or exposure to ionising radiation. This makes it particularly suitable for individuals with limited intravenous access, as well as for vulnerable populations including infants, children, and pregnant women. In ASL, arterial blood water serves as an endogenous, diffusible tracer, with magnetically labelled inflowing blood used to generate perfusion contrast. The ASL signal is influenced by T_1 relaxation time of blood and the labelling decays after a long delay time (Detre et al. 1992; Haller et al. 2013).

To optimise signal quality and ensure sufficient delivery of labelled blood, ASL-MRI is generally acquired with pulse sequences that feature short TE and long

TR. This approach facilitates the quantitative estimation of the absolute value of cerebral blood flow, enabling the evaluation of various neurological conditions, including Alzheimer's disease and mild cognitive impairment (Jahng et al. 2014).

Other types of MR images include structural MRI and functional MRI (fMRI). Static structural MRI is used to acquire high-resolution anatomical images that show the shape, size, and spatial organisation of tissues and organs. fMRI evaluates brain activity by detecting changes in blood flow and oxygenation levels, reflecting neuronal activation. Beyond perfusion MRI, advanced techniques, such as diffusion weighted imaging (DWI) and proton MR spectroscopy (MRS), offer complementary information. Although not perfusion methods, DWI and MRS, when used in combination, contribute to a comprehensive multiparametric assessment of brain tumours and other pathological conditions (Symms et al. 2004; Cecil 2013; McGarry et al. 2022). This thesis will focus primarily on the combination of DSC- and DCE-MRI techniques. A summary of the key characteristics, imaging parameters, and typical clinical applications of DSC- and DCE-MRI is provided in Table 2.1.

Table 2.1: Summary of exogenous CA-based MR perfusion techniques (Jahng et al. 2014).

	DSC-MRI	**DCE-MRI**
Imaging Types	T_2 or T_2^*-weighted imaging	T_1-weighted imaging
Imaging Parameters[1]	Long TR (200-800 ms) Long TE (20-50 ms) Intermediate θ (30-50°)	Short TR (5-10 ms) Short TE (2-5 ms) Small θ (5-20°)
Acquisition Point	First pass of CA	Accumulation of CA
Acquisition Duration	Relatively short (< 2 min)	Long ($\approx$ 5 to 6 min)
Signal Contribution	Change in T_2/T_2^* relaxation	Change in T_1 relaxation
Signal Profiles[2]		
Signal Images[2]		
Perfusion Parameters[3]	CBV, CBF, MTT	K^{trans}, k_{ep}, v_e
Clinical Applications	Brain (most), stroke, tumour	Brain, breast, prostate

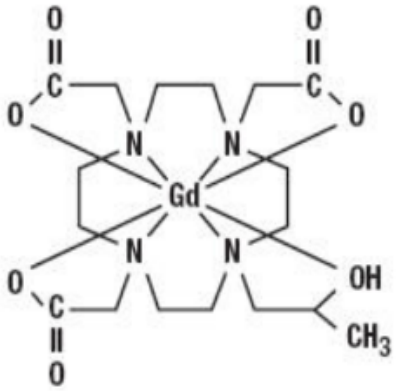
[1] Imaging parameter ranges are specified for a 1.5 Tesla system.
[2] Signal profiles and images are derived from a patient in the ACRIN-6684 dataset.
[3] A detailed discussion of perfusion parameters is provided in chapter 4.

2.5 Contrast Agents

The CAs play a crucial role in DSC- and DCE-MRI by enhancing image clarity and detail, thereby improving the differentiation between various tissues and highlighting specific anatomical structures within the body. The most commonly utilised agents are highly water-soluble gadolinium chelates, represented by the chemical symbol Gd, such as gadoterate meglumine (Gd-DOTA) and gadoteridol (Gd-HP-DO3A). Figure 2.11 presents gadoteridol and its chemical structure, adapted from the Bracco website[3]. The use of gadolinium-based agents is attributed to their seven unpaired electrons, which endow them with a strong paramagnetic property, making them highly effective for enhancing MRI signals (Dance et al. 2014). Between 1995 and 2017, six gadolinium-based CA received approval from the FDA for clinical application (Ibrahim et al. 2023).



(a) A gadoteridol with the brand name ProHance®.



(b) The structural formula of gadoteridol.

Figure 2.11: A gadolinium-based contrast (gadoteridol with empirical formula of $C_{17}H_{29}N_4O_7Gd$) manufactured by Bracco Diagnostics Inc.

[3] https://www.bracco.com/sites/default/files/2024-04/prohance_package-insert_english.pdf

Gadolinium-based CAs are administered via the intravenous route, with an FDA-approved standard dosage of 0.1 mmol/kg during a single imaging session. However, this dosage may vary depending on the specific imaging protocol and patient considerations. For example, gadoxetic acid, a liver-specific CA, is typically administered at a dose of 0.025 mmol/kg (Cheong et al. 2022).

In structural MRI, CAs are particularly useful for highlighting vascular structures such as arteries and veins, thereby aiding in the detection of abnormalities, including aneurysms, stenosis, and thrombosis. In contrast, the use of CAs in DSC- and DCE-MRI is not merely beneficial but essential. Both techniques rely on pharmacokinetic (PK) analysis of CAs derived concentration time curves to quantify tissue blood flow dynamics. This approach is critical for assessing cerebral and cardiac perfusion in both clinical and research settings (Tircsó et al. 2021; McLeod et al. 2021).

2.6 Advantages and Disadvantages of MRI

According to the FDA (2017), MRI scanners possess the capability to acquire images of any region of the body, including the head, joints, abdomen, and legs, in any orientation. Compared to CT, MRI provides superior soft tissue contrast, facilitating clearer differentiation between various tissue types such as fat, water, and muscle. While CT is particularly adept at imaging bones, MRI is more effective for visualising soft tissues. These detailed images are instrumental for physicians in diagnosing a wide array of medical conditions and diseases.

However, there are notable safety concerns associated with MRI procedures due to the use of static or varying magnetic fields and RF energy. For instance, patients may experience potential hearing impairment from the loud knocking noises produced during scanning, and RF energy can lead to localised heating of body tissues. Additionally, the use of CAs in MRI carries inherent risks, including allergic reactions and the potential for kidney toxicity (Martino et al. 2021).

While MRI provides a diverse array of functionalities, it is frequently utilised in conjunction with other imaging modalities, such as CT and PET. The PET-MRI scanner exemplifies a hybrid imaging technology that merges the morphological imaging capabilities of MRI, which excels at soft tissue visualisation, with the metabolic and functional imaging provided by PET. This integrated approach enables simultaneous acquisition of imaging data, thereby reducing overall scanning time and enhancing the precise localisation of both functional and structural abnormalities (Antoch et al. 2009).

University College Cork, Ireland
Coláiste na hOllscoile Corcaigh

CORA
Cork Open Research Archive
Cartlann Taighde Oscailte Chorcaí

Hu, Y. 2025. A statistical re-examination of the spoiled gradient recall echo equation in the analysis of data from DSC and DCE MR imaging procedures. PhD Thesis, University College Cork.

Please note that Chapter 3 (pp. 35-96) is unavailable due to a request by the author.

CORA Cork Open Research Archive http://cora.ucc.ie

Chapter 4

Pharmacokinetic Modelling

Following the conversion of signal intensity to CA concentration, pharmacokinetic (PK) modelling is performed to quantify the spatial-temporal distribution of CA within tissues of interest, with particular emphasis on characterising tumour pathophysiology. Parametric maps derived from PK analysis, such as perfusion, permeability, and extracellular volume fraction, are used to non-invasively monitor disease progression and therapeutic efficacy in diverse pathological conditions, including ischemia, inflammatory disorders, malignancies, and metabolic diseases.

This chapter provides a systematic review of the methodological framework for semi-quantitative and quantitative analyses in DSC- and DCE-MRI. Key components, including theoretical assumptions, PK model derivation and selection, and the common objective of quantitative analyses in both image protocols, are discussed.

4.1 Modelling in DSC-MRI

Analysis methods for DSC-MRI broadly fall into two categories: semi-quantitative and quantitative techniques. Semi-quantitative approaches, while computationally simple and time-efficient, lack direct physiological interpretability. In contrast, quantitative approaches utilise PK models to derive biological parameters, such as cerebral blood volume (CBV) and cerebral blood flow (CBF).

Furthermore, once the CA concentration is provided, PK models commonly used in DCE-MRI, such as the extended Tofts and Kermode model (described in subsubsection 4.2.3.2), can also be applied to DSC-MRI for estimating relevant perfusion parameters. Because PK modelling characterises the distribution of CAs in the body, reflecting underlying tumour biology, it is independent of the imaging protocol (e.g., DSC- or DCE-MRI) and, more broadly, of the imaging modality itself, whether CT or MRI (Tofts 2010). However, the accuracy of quantitative models relies heavily on their underlying assumptions, which may not universally hold across different tissues or tumour types. Therefore, selecting an appropriate PK model requires careful consideration of the specific clinical scenario (Buckley 2002).

4.1.1 Semi-quantitative Method

The semi-quantitative (or model-free) approach calculates empirical indexes based on the temporal profile of the signal intensity time course, $S(t)$. Accordingly,

it does not require the reconstructing CA concentration methods discussed in chapter 3, either for DSC- or for DCE-MRI. Figure 4.1 illustrates three main stages of signal intensity in DSC-MRI: the baseline period (T_o), the first passage of the CA (from T_o to T_s), and the recirculation phase (from T_s to T_r).

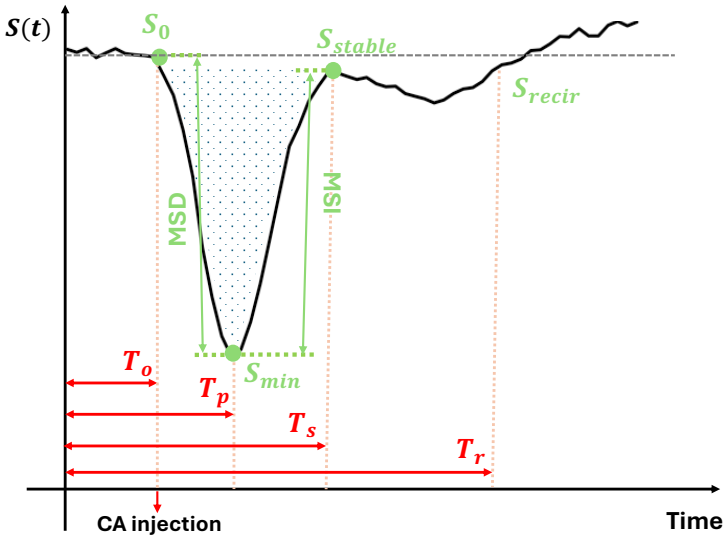


Figure 4.1: The summary parameters of semi-quantitative approach in DSC-MRI (Paulson et al. 2008; Essock-Burns et al. 2013).

The baseline parameter T_o, also referred to as contrast arrival time, is defined as the time interval from CA injection to its initial detection in the tissue. The corresponding baseline signal intensity is denoted by S_0. Following the injection, the signal rapidly decreases to its minimum, S_{min}. The time required to reach this minimum is referred to as the time to negative peak (TTP), defined as $T_p - T_o$. The maximum signal drop (MSD) is given by $S_0 - S_{min}$. Subsequently, as the signal begins to return toward a stable level S_{stable}, the maximum signal increase (MSI) is defined as $S_{stable} - S_{min}$. The area under the first passage of the signal curve (illustrated by the blue dots in Figure 4.1) is termed the negative

enhancement integral (NEI), which reflects the total CA passage through the regional vasculature and serves as an approximate measure of blood volume. The mean time to enhance (MTE) represents the average transit duration of the entire contrast bolus through the tissue, and is conceptually distinct from the mean transit time (MTT), which characterises the average duration of individual contrast molecules. Computational simulations reveal MTE values may exceed true MTT by up to threefold (Essock-Burns et al. 2013; Bian et al. 2020). A comprehensive summary of these parameters, including interpretations and units, is provided in Table 4.1.

Table 4.1: The summary parameters for semi-quantitative in DSC-MRI.

Parameter	**Description**	**Units**
$\boldsymbol{T_o}$	contrast arrival time	sec
$\boldsymbol{TTP}$	Time to negative peak, T_p	sec
$\boldsymbol{NEI}$	Negative enhancement integral, $\int_{T_o}^{T_s} S(t)dt$	Arbitrary Units
$\boldsymbol{MTE}$	Mean time to enhance, $T_p - T_o$	sec
$\boldsymbol{MSD}$	Maximum signal decrease, $S_0 - S_{min}$	Arbitrary Units
$\boldsymbol{MSI}$	Maximum signal increase, $S_{\text{stable}} - S_{min}$	Arbitrary Units

The primary advantage of the semi-quantitative approach is simplicity. This approach avoids the need for arterial input function (AIF) measurements and directly estimates parameters from the $S(t)$ time course, eliminating the requirement for CA concentration conversion. Therefore, it is widely adopted in clinical applications. However, their inherent limitations, including susceptibility to acquisition protocols and reproducibility issues, highlight the need for quantitative

PK modelling to balance computational efficiency with physiological accuracy (Perthen et al. 2002).

4.1.2 Quantitative Methods

Quantitative approaches employ PK models to analyse tissue concentration time course $C_t(t)$, enabling the estimation of physiologically relevant parameters that reflect tissue vascularity and function. The quantitative perfusion analysis in DSC-MRI relies on kinetic modelling and can be expressed as:

$$\Delta R_2^*(t) \propto C_t(t) = f \cdot C_b(t) \otimes R(t) \tag{4.1}$$

where, f is blood flow and $\otimes$ represents the convolution operator. $C_b(t)$ refers to the whole-blood concentration and is related to the plasma concentration $C_p(t)$ through the haematocrit (Hct), which is assumed to be constant at 0.42, such that $C_b(t) = (1 - Hct)C_p(t)$. The reason for using $C_b(t)$ is that the distinction accounts for differential CA distribution between plasma and erythrocytes under circulatory dynamics (Barbier 2013). $R(t)$ is a residue function characterising CA retention dynamics.

This modelling framework enables DSC-MRI to quantify three key haemodynamic parameters: (1) cerebral blood volume (CBV), which quantifies the total blood

volume within cerebral microvasculature (unit: mLg^{-1}); (2) cerebral blood flow (CBF), which measures the rate of blood flow per unit of brain tissue (unit: $\text{mLg}^{-1}\text{min}^{-1}$); and (3) mean transit time (MTT), which represents the average capillary passage duration of blood (unit: sec). Elevated CBV values correlate with tumour neoangiogenesis and have prognostic significance for grading and treatment response monitoring (Aronen et al. 2000). In DSC-MRI, two distinct methodologies enable CBV quantification as illustrated in 3(a) and 3(b) of Figure 4.2. The first approach calculates CBV through the integral ratio between $C_t(t)$ and blood concentration $C_b(t)$:

$$CBV = \frac{k_h \int_0^\infty C_t(t)dt}{\rho \int_0^\infty C_b(t)dt} \tag{4.2}$$

where ρ represents tissue density and k_h is a correction factor accounting for differences between capillary and large vessel haematocrit, which can be calculated as $k_h = (1 - 0.45)/(1 - 0.25)$ (Rempp et al. 1994; Perthen et al. 2002).

The second methodology, which requires the measurement of blood concentration $C_b(t)$, employs compartmental models or deconvolution techniques to estimate the residue function $R(t)$ and the absolute perfusion parameters. In Equation 4.1, the flow f is defined as $f = (\rho/k_h) \cdot CBF$. Since the residue function satisfies $R(0) \equiv 1$, f can be determined at $t = 0$, yielding CBF as:

$$CBF = \frac{k_h}{\rho} f \tag{4.3}$$

The MTT is defined as the integration of $R(t)$ and thus, the CBV can be derived from the central volume principle of indicator-dilution theory, yielding $CBV = MTT \cdot CBF$ (Zierler 1962; Roberts et al. 1973).

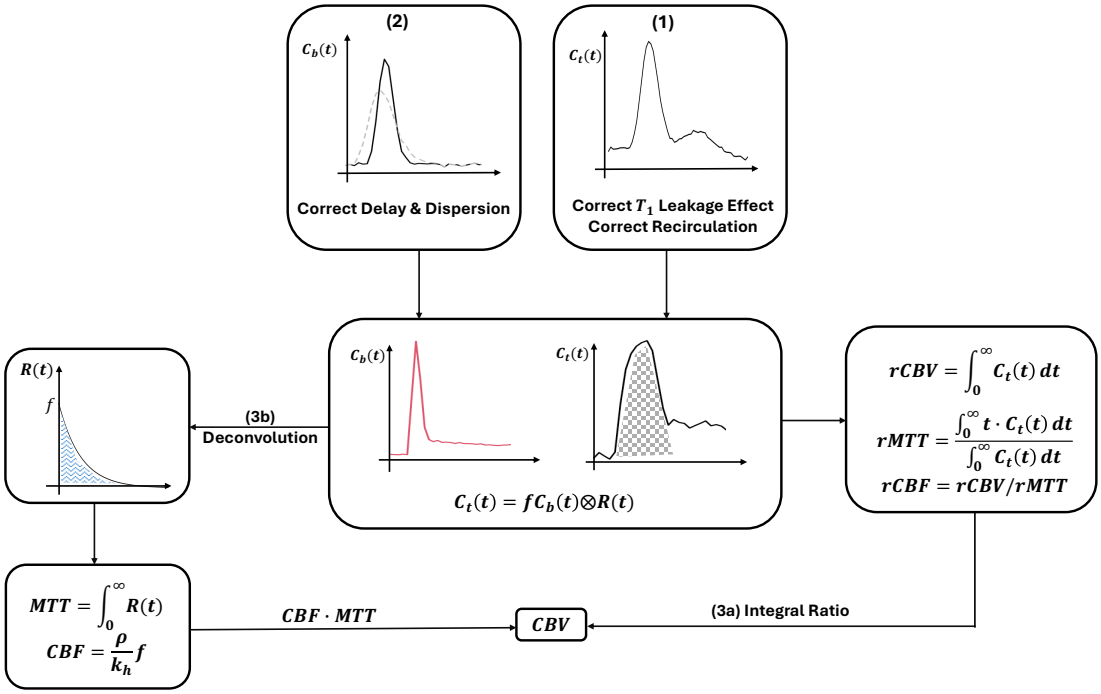


Figure 4.2: CBV quantification workflow: the pre-processing step (1) addresses CA leakage effects and eliminates recirculation; and step (2) removes dispersion/delay in $C_b(t)$. The step (3a) is the integral ratio method that calculates $rCBV$ as the area under the $C_t(t)$ curve (grey shaded), with $rMTT$ derived from the curve's normalised first moment. The absolute CBV is determined via Equation 4.2. In contrast, the deconvolution method (Step 3b) derives the $R(t)$ from the measurement of blood concentration $C_b(t)$. Absolute MTT is obtained through $R(t)$ integration, absolute CBF is proportional to the peak amplitude f of $R(t)$, and absolute CBV is ultimately determined via the central volume principle (Grøvik et al. 2020).

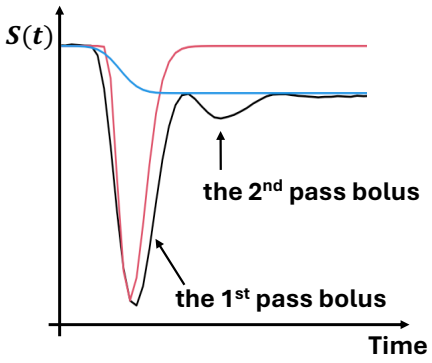
4.1.3 Corrections in Concentration of DSC-MRI

The quantitative accuracy of DSC-MRI depends on three critical corrections. First, the T_1 shortening effects from CA extravasation must be negligible. This phenomenon manifests as either signal recovery exceeding baseline levels (as illustrated in $S(t)$ after T_r in Figure 4.1) or negative values in concentrations (as illustrated in (1) of Figure 4.2). Consequently, the estimations of CBV and CBF are inaccurate and imprecise. The correction strategies include CA-relevant, such as pre-loading and post-processing algorithms correction (Boxerman et al. 2012).

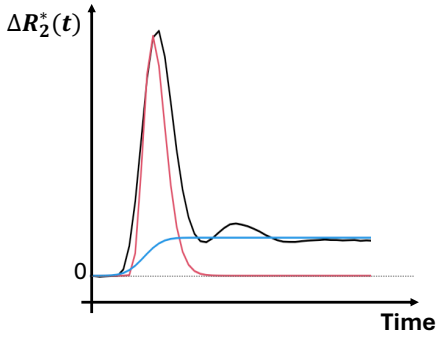
The pre-loading technique has been widely adopted in DSC-MRI protocols to reduce the T_1 shortening effect. This method involves administering 1/4 to 1/3 of the total CA dose prior to DSC image acquisition, thereby minimising subsequent changes in T_1 relaxation (Welker et al. 2015). However, the exact dose of pre-loading is unknown, and the technique only partially mitigates the T_1 shortening effect, leaving residual contamination in the DSC signal dynamics (Donahue et al. 2000; Schmainda et al. 2004). Therefore, pre-loading is typically used in conjunction with model-based post-processing correction algorithms, such as the Gamma-variate function (GVF), to more effectively reduce leakage effects. The combination of these methods improves the accuracy of perfusion parameter estimation in DSC-MRI (Boxerman et al. 2012).

Second, absence of CA recirculation, requiring $C_t(t)$ to demonstrate monophasic first-pass kinetics without secondary contrast reappearance. The recirculation effect in DSC arises from the redistribution of CA through renal and coronary

circulations following initial bolus clearance, manifesting as secondary CA passage through tissue (as illustrated in Figure 4.3a). This phenomenon prevents signal return to its original baseline, leading to contamination of $\Delta R_2^*(t)$ measurements that underestimates $rCBV$ by distorting contrast clearance kinetics (Jerrold L Boxerman et al. 1997).



(a) Recirculation in $S(t)$. The black curve represents the DSC signal, the red and blue curves represent the first pass arterial and recirculation, respectively.



(b) Recirculation in $\Delta R_2^*(t)$. The black curve represents $\Delta R_2^*(t)$, the red is modelled by GVF, and the blue curve is the cumulative integral.

Figure 4.3: Illustration of recirculation effect. The curves are derived from a patient in the ACRIN-6684 dataset, as discussed in chapter 3.

Model-based analytical approaches, such as the GVF, are employed to mitigate the recirculation effect. The GVF acts as a post-processing tool to isolate first-pass haemodynamics by modelling $C_t(t)$, thereby eliminating recirculation and leakage effects occurring after the initial bolus passage. While GVF proves effective in eliminating recirculation, it has two critical limitations: first, its sensitivity to noise; and second, its computational expense and dependence on initial values. Consequently, the American Society of Functional Neuroradiology (ASFNR) guidelines recommend direct integration over the acquired $C_t(t)$ rather than GVF fitting for clinical brain perfusion analysis (Benner et al. 1997; Welker et al. 2015;

Paulson et al. 2016; Hu et al. 2021).

Third, no dispersion or delay in AIF estimation, as the black curve in (2) of Figure 4.2 (Jahng et al. 2014). Since the AIF is typically obtained from a major artery, such as the internal carotid artery or middle cerebral artery (MCA), the transit of the contrast bolus from these arteries to the ROI can introduce bolus delay and dispersion. These effects lead to significant errors in parameter estimation, for example, underestimation of CBF and overestimation of MTT (Fernando Calamante et al. 2000; Petrella et al. 2000; Calamante et al. 2002). In such cases, the shape of the residue function $R(t)$ is influenced by both vascular and tissue properties, represented as the effective residue function, $R^{eff}(t)$. Figure 4.4 illustrates a comparison between the corrected $R^{eff}(t)$ (black) and cases where delay or dispersion occurs, highlighting their impact on perfusion parameter estimation.

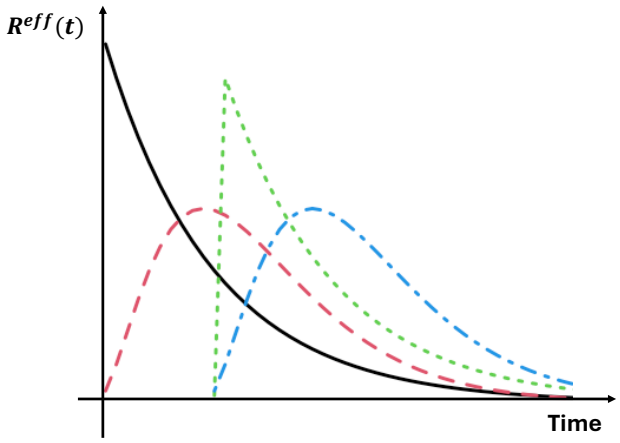


Figure 4.4: An example of the effective residue function $R^{eff}(t)$: The black curve represents both delay and dispersion corrected; the green curve accounts for dispersion correction only; the red curve corrects for delay only; and the blue curve remains uncorrected for both delay and dispersion (Willats et al. 2008).

Various methods have been proposed to correct or mitigate errors associated with bolus delay, including using a local AIF and modelling delay as an additional parameter. The local AIF method involves selecting multiple small arteries adjacent to the ROI or using a regional AIF. However, this approach is relatively recent in the history of DSC-MRI and is subject to partial volume effects, which can influence accuracy. Furthermore, its validation remains controversial (Lisa Willats et al. 2011; Fernando Calamante 2013). Alternatively, bolus delay can be explicitly incorporated as an additional parameter during modelling, as seen in Bayesian-based methods (Mouridsen et al. 2006) and iterative approaches (Lisa Willats et al. 2006).

As illustrated in Figure 4.4, the $R(t)$ shape can become distorted during CA transit through the arterial system due to dispersion. The degree of dispersion significantly impacts CBF quantification, leading to varying degrees of underestimation, potentially up to 70% (Fernando Calamante et al. 2006). A potential solution to this problem is using the local AIF methods. An alternative approach involves modelling the AIF using a vascular transport function (VTF), which imposes a peaked shape with a lower maximum than the true residue function, as illustrated by the green curve in Figure 4.4. However, the underlying assumptions of this method may not be valid for all patients in general clinical settings (Fernando Calamante 2005; Fernando Calamante et al. 2006).

4.1.4 Summary of DSC-MRI Analysis

Following rigorous validation of the three fundamental assumptions in DSC modelling, quantitative estimation of CBF, CBV, and MTT becomes feasible. Nevertheless, variations in analytical methods across commercial software platforms, such as the distinct approaches labeled (3a) and (3b) in Figure 4.2 within NordicICE and GE BrainStat, significantly affect the consistency of perfusion measurements. Specifically, methods incorporating AIF selection introduce greater variability in parameter estimates, limiting direct comparability between single-centre and multi-centre studies. To address this challenge, simplified analytical techniques relying on direct analysis of the raw tissue $C_t(t)$ curve have demonstrated improved stability and reproducibility in clinical settings (Orsingher et al. 2014).

The clinical utility of DSC-MRI extends beyond neuroimaging to oncological applications in breast and rectal cancer. However, these implementations require specialised acquisition protocols and post-processing corrections to reduce CA leakage effects. Dual-echo and multi-echo sequences have emerged as effective solutions, enabling concurrent acquisition of DSC and DCE data with a single CA injection (Grøvik et al. 2014; Grøvik et al. 2017). Validation studies in human skeletal muscle perfusion and quantification of perfusion changes during hyperemia have established the technical feasibility of these integrated approaches (Englund et al. 2013; Grøvik et al. 2014). Key parameters of DSC-MRI quantification in this chapter are summarised in Table 4.2.

Table 4.2: Quantitative DSC-MRI parameters.

Parameter	Description	Units
CBV	Blood volume	mLg^{-1}
CBF	Blood flow	$\text{mLg}^{-1}\text{min}^{-1}$
MTT	Mean transit time	sec
Hct	Haematocrit constant, 0.42	Arbitrary Units
k_h	Correction factor for Hct, 0.73	Arbitrary Units

4.2 Modelling for DCE-MRI

Like DSC-MRI, DCE-MRI analysis incorporates both semi-quantitative approaches, which rely on signal intensity, and quantitative methods, which are based on converted contrast agent concentration.

4.2.1 Semi-quantitative Method

Baseline parameters T_o (contrast arrival time) and TTP (time-to-peak: $T_p - T_o$) are defined similarly in both DSC- and DCE-MRI, as illustrated in Figure 4.5. While DCE introduces some unique summary parameters, such as wash-in slope, wash-out slope, AUC, and $IAUC$. The wash-in and wash-out slopes denote the gradients of the lines connecting S_0 to S_{max} and S_{max} to S_{final}, respectively. The total area under $S(t)$ is termed area under the curve (AUC), analogous to the NEI in DSC-MRI, while the area under the initial uptake phase, indicated by blue dots, is termed the initial AUC, $IAUC$ (F. Khalifa et al. 2014). These parameters are summarised in Table 4.3.

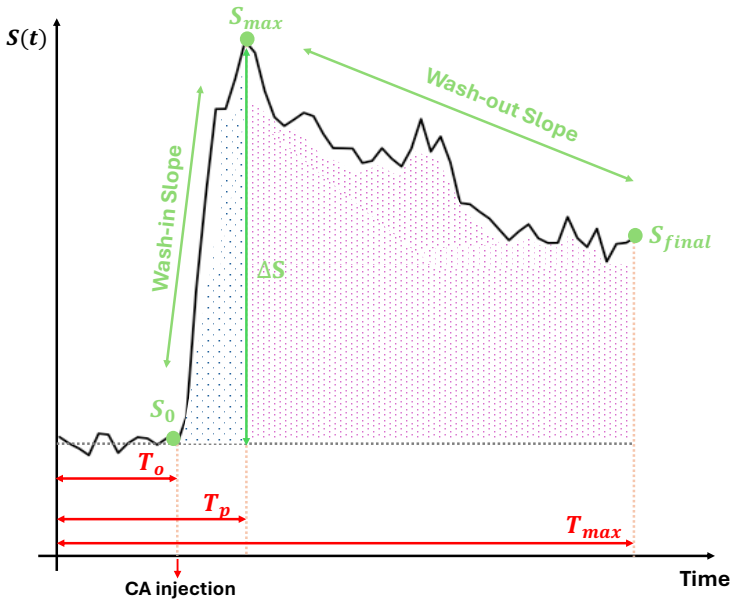


Figure 4.5: The summary parameters of semi-quantitative approach in DCE-MRI (F. Khalifa et al. 2014).

Table 4.3: The summary parameters for semi-quantitative in DCE-MRI.

Parameter	Description	Units
$\boldsymbol{T_o}$	Onset time of an enhancement curve	sec
$\boldsymbol{TTP}$	Time to peak, $T_p - T_o$	sec
$\boldsymbol{\Delta S}$	Maximal contrast enhancement, $S_{\max} - S_0$	Arbitrary Units
Wash-in Slope	$\Delta S/(T_p - T_o)$	$\sec^{-1}$
Wash-out Slope	$(S_{\max} - S_{\text{final}})/(T_{\max} - T_p)$	$\sec^{-1}$
$\boldsymbol{AUC}$	Area under curve, $\int_{T_o}^{T_{max}} S(t)dt$	Arbitrary Units
$\boldsymbol{IAUC}$	Area under the initial uptake, $\int_{T_o}^{T_p} S(t)dt$	Arbitrary Units

Similar to DSC-MRI, semi-quantitative parameters in DCE-MRI are categorised for simplicity and clinical practicality, allowing for rapid assessment. As a result, this method is widely adopted in clinical applications, such as myocardial perfusion imaging and prostate cancer. Nevertheless, because these summary parameters are derived directly from raw signal intensity, they are inherently sensitive to variations in acquisition protocols and scanner hardware. Consequently, reproducibility across different platforms or multi-centre studies remains a significant limitation (Paldino et al. 2009; O'connor et al. 2011; Isebaert et al. 2012; Tarroni et al. 2012).

4.2.2 Quantitative Models

Compartmental models, which are typically employed in the quantitative analysis of DCE-MRI, are fundamentally concentration-based. As such, they can also be adapted for use in DSC-MRI quantification. A schematic overview of PK parameter derivation in both image protocols is provided in Figure 4.6.

The measurement or estimation of the CA concentration in the blood plasma ($C_p(t)$) is a challenge in both DSC- and DCE-MRI. Unlike tissue concentration, an ideal AIF profile should exhibit a rapid initial uptake followed by a narrow, well-defined peak, as the red curve in step (2) of Figure 4.6 (Fernando Calamante 2010). However, measurement accuracy is often compromised by flow artifacts, inflow effects, and nonlinear effects caused by high local CA concentrations (Geoff JM Parker et al. 2006).

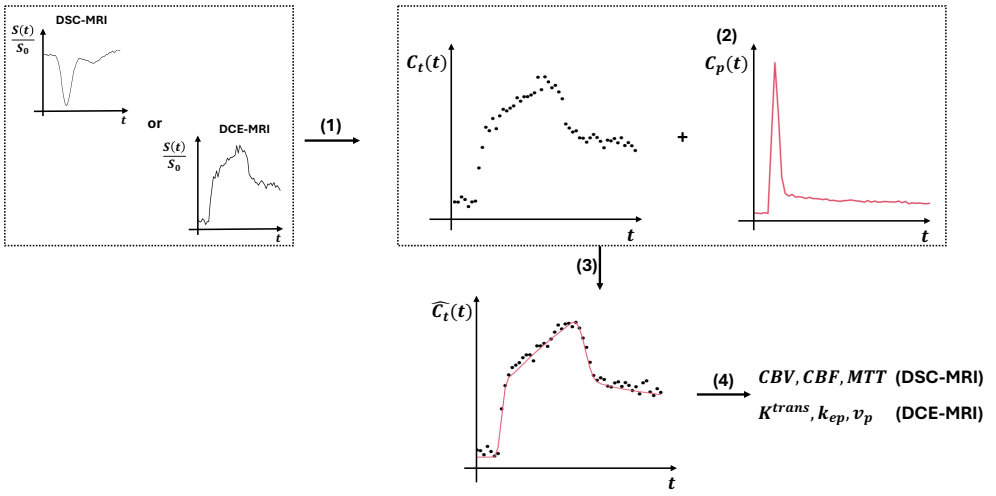


Figure 4.6: Procedure of quantitative analysis: (1) Convert the signal intensity to CA concentration based on the relative signal intensity; (2) Define AIF; (3) Fit model to concentration curve; and (4) estimate the PK parameters (Bernstein et al. 2014).

4.2.3 Compartmental Models

Compartment models have gained widespread adoption in PK analysis due to their conceptual simplicity and minimal parameter requirements. Originally developed to investigate blood-brain barrier (BBB) permeability, these models now serve as foundational tools for DCE-MRI across diverse clinical applications. Seminal works by Larsson, Brix, and Tofts established their utility in characterising CA kinetics in neurological disorders (Larsson et al. 1990; Brix et al. 1991; Tofts et al. 1991).

Compartmental models mathematically describe CA exchange between blood and tissue over time. Here, a "compartment" is conceptualised as a well-mixed bucket where CA concentration remains spatially uniform. Key assumptions include: (1) homogeneity (well-mixed), i.e., instantaneous mixing ensures uniform

CA distribution within each compartment at any given time; (2) linear transport, i.e., inter-compartmental flux is proportional to concentration gradients; (3) time invariance, i.e., the PK parameters describing the compartments remain constant during imaging (Tofts 1997). While increasing compartment numbers improves model accuracy, it escalates computational complexity (Cobelli et al. 1992). The two-compartment (2C) model, balancing simplicity and biological plausibility, dominates clinical DCE-MRI analyses.

As illustrated in Figure 4.7, the 2C model partitions the CA distribution into two interconnected pools: the intravascular space and the extracellular extravascular space (EES) or interstitial water (cytoplasmic) space. Upon CA administration, it rapidly distributes within plasma, denoted as $C_p(t)$. Then, it passively diffuses across the vascular endothelium into EES at a rate K_1 and refluxes at a rate K_2 since CA cannot be taken into cells. Thus, the time-varying concentration in the EES is represented as $C_e(t)$. The dimensionless fractional volume v_e (EES occupancy) and v_p (plasma occupancy) both range from 0 to 1, reflecting their proportional contributions to total tissue volume. Renal clearance ultimately removes CA from circulation (Tofts 1997).

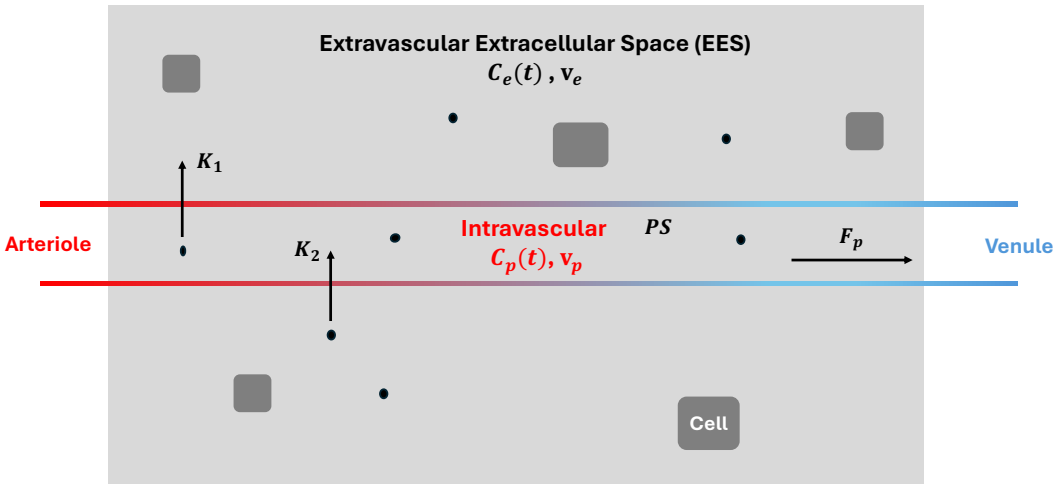


Figure 4.7: Schematic illustration of 2C model. The light-grey background represents a tissue, divided into intravascular (blood plasma) and EES compartments. Black dots are CA molecules that passively diffuse across capillary walls into the EES and reverse, driven by concentration gradients. However, CA cannot enter the intracellular space (Bernstein et al. 2014). Notably, the illustrated proportions of plasma volume fraction (v_p) and extracellular volume fraction (v_e) are schematic representations rather than physiologically accurate scales. These proportions remain the same throughout this chapter's schematic illustration.

Similar to quantitative analysis in DSC-MRI, the fundamental kinetic equation underlying DCE-MRI perfusion models expresses tissue concentration, $C_t(t)$, in any linear stationary system as:

$$C_t(t) = f \cdot C_p(t) \otimes R(t) \tag{4.4}$$

where f is blood flow, $C_p(t)$ is the AIF, $\otimes$ represents the convolution operator and $R(t)$ is a residue function characterising CA retention dynamics. The residue function is derived from compartmental models that encode tissue-specific physiological interactions (Zierler 1962; Jerosch-Herold et al. 1998).

Although the Larsson and Brix models were among the earliest PK models developed for DCE-MRI analysis (Larsson et al. 1990; Brix et al. 1991), the Tofts–Kermode (TK) model and its extended variants have since become the gold standard for clinical applications. Their widespread adoption in oncology has enabled the characterisation of tumours across a range of malignancies, including those in the brain, lung, breast, and prostate (Hunter et al. 1998; S. P. Sourbron et al. 2011; Xia Li et al. 2012). This thesis primarily focuses on the TK and ETK models, while also summarising alternative PK models, particularly in cases where the assumptions underlying the TK model are not satisfied.

4.2.3.1 Tofts and Kermode Model

The TK model, introduced in 1991 by Tofts, Kermode, and colleagues, provides a PK framework for quantifying perfusion and vascular permeability in DCE-MRI. As a variant of the 2C model, the framework of the TK model diverges from conventional compartmental approaches by explicitly modelling BBB disruption. Under such conditions, an additional lesion compartment is introduced to represent CA leakage through compromised endothelial membranes, as schematised in Figure 4.8 (Tofts et al. 1991; Tofts 2010).

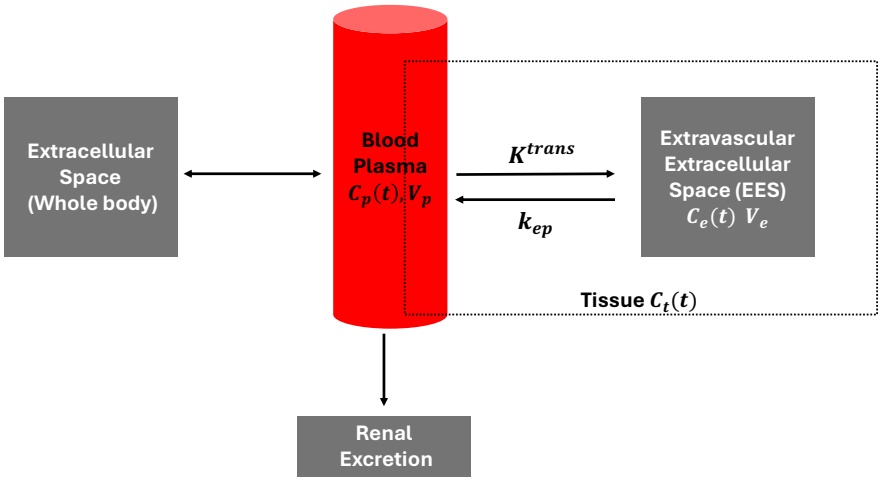


Figure 4.8: Schematic illustration of TK model: in the lesion leakage space (dashed box), the CA transfer between intravascular and extracellular space with rate K^{trans} and k_{ep}, respectively (Tofts 2010).

In the TK model, the amount of CA in the leakage space is $v_e V_t C_e$, where V_t denotes the total lesion tissue volume. The exchange of CA between plasma and the lesion leakage space is governed by:

$$v_e V_t \frac{dC_e(t)}{dt} = PS(C_p(t) - C_e(t)) \tag{4.5}$$

where, P corresponds to the membrane permeability coefficient, while S represents the surface area of the leaky membrane. This equation assumes that CA flux is proportional to both the membrane surface area and the concentration gradient across the membrane. Rearranging Equation 4.5 yields:

$$v_e \frac{dC_e(t)}{dt} = k(C_p(t) - C_e(t)) \tag{4.6}$$

where $k = PS/V_t$ defines the permeability–surface area product per unit tissue volume (unit: min^{-1}) (Davson et al. 1987). In the TK model, this parameter is commonly expressed as the volume transfer constant K^{trans}. Importantly, K^{trans} reflects the combined effect of both the permeability–surface area product (PS) and the blood plasma flow f, since PS and f cannot be independently measured under this model. Analogously, K^{trans} corresponds to the influx constant K_i in PET imaging (Tofts et al. 1991).

In the TK model, the intravascular contribution is typically small ($v_p \approx 1 - 10\%$) and often neglected. Thus, the total tissue concentration predominantly reflects leakage space contribution, i.e., $C_t(t) = v_e C_e(t)$. Substituting this relationship

into Equation 4.6 gives:

$$\frac{dC_t(t)}{dt} = K^{trans}C_p(t) - k_{ep}C_t(t) \quad \Rightarrow \tag{4.7}$$
$$C_t(t) = K^{trans}\int_0^t C_p(\tau)e^{-k_{ep}(t-\tau)}d\tau$$

where $k_{ep} = K^{trans}/v_e$ denotes the reflux rate constant. In the TK model, the Equation 4.4 can thus be rewritten as:

$$C_t(t) = K^{trans} \cdot C_p(t) \otimes e^{-k_{ep}(t)} \tag{4.8}$$

where the residue function denoted as $R(t) = e^{-k_{ep}(t)}$. The voxel-wise estimation of K^{trans} and k_{ep} can be obtained through nonlinear least squares fitting algorithms (Tofts et al. 1991).

4.2.3.2 Extended Tofts and Kermode Model

When accounting for intravascular contributions, particularly in malignant tumours and other highly vascular lesions, the extended Tofts-Kermode (ETK) model enhances tissue concentration characterisation through explicit inclusion of the

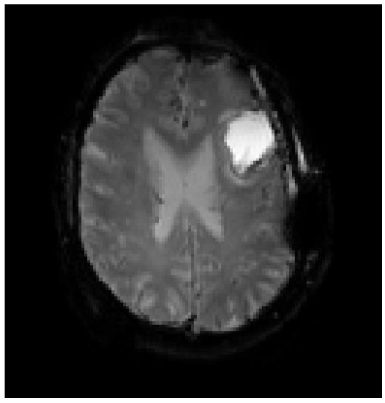
vascular term $v_p C_p(t)$. The ETK formulation expresses total tissue concentration as (Tofts 2010):

$$C_t(t) = v_p C_p(t) + K^{trans} \int_0^t C_p(\tau) e^{-k_{ep}(t-\tau)} d\tau \tag{4.9}$$

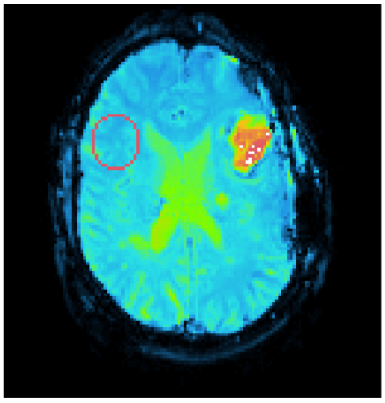
Model selection between the TK and the ETK models hinges on tissue vascular characteristics. Specifically, the TK model is particularly suitable for analysing tissues with limited vascularisation, where intravascular signal contributions are minimal. Conversely, the ETK model is essential for highly perfused tissues where blood volume significantly modulates CA kinetics. Both models demonstrate comparable fitting performance in tissues with extreme blood volume profiles or extreme speed of CA exchange, though parameter interpretation becomes ambiguous under these conditions. Conversely, neither model adequately captures concentration dynamics in tissues with intermediate vascularity/permeability (S. P. Sourbron et al. 2011). Additionally, the transfer constant K^{trans}, which incorporates both the blood flow (F_b) and permeability surface area product (PS), is challenging to disentangle during estimation. Although these constraints exist, the TK and ETK models remain clinically validated frameworks for DCE-MRI perfusion analysis.

As previously noted, PK models can be applied to both DSC- and DCE-MRI, as their applicability depends on CA concentration rather than imaging modality. Figure 4.9 presents the ETK model application to DSC-MRI data from the same

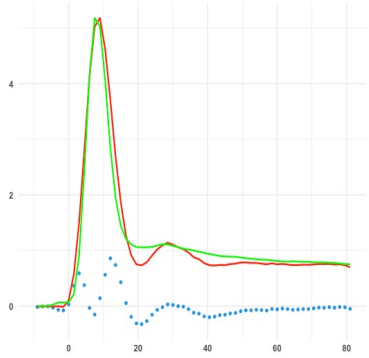
patient described in chapter 3, acquired from the ACRIN-6684 dataset. For anatomical reference and ROI localisation, a baseline scan is shown in Figure 4.9a. The corresponding dynamic signal image is shown in Figure 4.9b. The red circled area indicates the normal region, located contralateral to the tumour. The average relative signal intensity from this region was used to derive the $S(t)/S_0$ time course. After applying a negative logarithmic transformation (Equation 3.2), the reconstructed concentration time course $C_t(t)$ is shown as a red curve in Figure 4.9c, with the ETK model estimated $\hat{C}_t(t)$ in green and the residuals in blue dots. The resulting estimates of the perfusion parameters are summarised in Figure 4.9d. The corresponding DCE-MRI fitting results for the same patient are shown in Figure 4.10. As with the DSC analysis, the ROI is located contralateral to the tumour and indicated by the red circle (Figure 4.10b). Here, the reconstructed concentration $C_t(t)$ (red curve in Figure 4.10c) was derived using the MFA estimated $\hat{T}_{10}$ (Equation 3.7) and converted via Equation 3.5. The ETK fitted concentration $\hat{C}_t(t)$ is shown in green, and the residuals are again plotted as blue dots. The estimated perfusion parameters are presented in Figure 4.10d.



(a) Middle slice of the baseline whole-brain image used for anatomical reference and ROI localisation.



(b) The normal ROI (red circle) in the dynamic signal image at the mid-slice and mid-time frame.

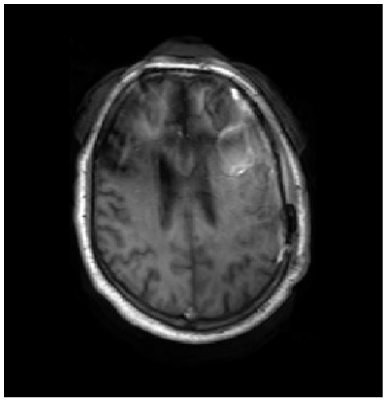


(c) The reconstructed concentration $C_t(t)$ (red curve) and the ETK fitted concentration $\hat{C}_t(t)$ (green curve), with blue dots representing the residuals between $C_t(t)$ and $\hat{C}_t(t)$.

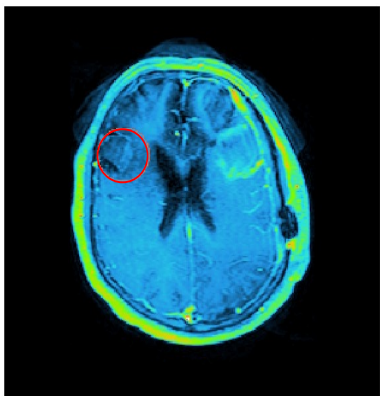
CBV	0.3
CBF	0.122
MTT	2.442

(d) The corresponding perfusion parameters estimated via the ETK model.

Figure 4.9: ETK model fitting in a normal brain region from DSC-MRI data of an ACRIN-6684 patient.



(a) Middle slice of the baseline whole-brain image used for anatomical reference and ROI localisation.



(b) The normal ROI (red circle) in the dynamic signal image at the mid-slice and mid-time frame.



(c) The reconstructed concentration $C_t(t)$ (red curve) and the ETK fitted concentration $\hat{C}_t(t)$ (green curve), with blue dots representing the residuals between $C_t(t)$ and $\hat{C}_t(t)$.

v_p	0.002
K^{trans}	0.000
k_{ep}	0.261

(d) The corresponding perfusion parameters estimated via the ETK model.

Figure 4.10: ETK model fitting in a normal brain region from DCE-MRI data of an ACRIN-6684 patient.

4.2.3.3 Other Models

The two-compartment exchange model (2CXM) was developed to independently quantify plasma flow (F_p) and permeability-surface area product (PS). Unlike the TK and ETK models, the 2CXM explicitly models both the intravascular and EES compartments while incorporating blood flow (Donaldson et al. 2010). Its main advantage is the ability to simultaneously estimate F_p, PS, and the volume fractions v_p, v_e (S. Sourbron et al. 2009).

When the assumption of infinitely fast transcytolemmal water exchange in conventional compartmental models is violated, the commonly assumed linear relationship between $C_t(t)$ and $R_1(t)$ may no longer hold. This can result in underestimation of K^{trans} and v_e, particularly in malignant breast tumours. To overcome this limitation, the shutter-speed model (SSM) introduces finite water exchange kinetics between compartments, allowing more accurate parameter estimation in heterogeneous tissues. The SSM further separates the extravascular space into the EES and the intracellular space (EIS), and models exchange between plasma, EES, and EIS. It incorporates the intracellular water residence time (τ_i) to account for distinct relaxation rates in the extracellular (R_{ie}) and intracellular (R_{1i}) compartments, yielding an effective relaxation rate R_1 (Landis et al. 2000; Xin Li et al. 2005; Huang et al. 2008).

In addition to conventional compartmental models that characterise temporal CA kinetics, advanced models such as the distributed-parameter (DP) model (Sangren et al. 1953) and the tissue-homogeneity (TH) model (J. A. Johnson

et al. 1966; Sawada et al. 1989) also account for spatial heterogeneity in perfusion parameters. Compared to traditional models, the DP model provides a more physiologically realistic representation of microcirculation by requiring fewer simplifying assumptions. However, this improved accuracy comes with increased computational complexity and a requirement for higher temporal resolution to yield reliable results (Kershaw et al. 2010).

4.2.4 Summary of DCE-MRI Analysis

A comprehensive overview of DCE-MRI analysis and modelling techniques has been presented, emphasising their diverse applications across various clinical studies. The semi-quantitative methods are straightforward to compute and easier to implement in routine clinical practice for diagnosis and staging. However, reproducibility remains a challenge, particularly when different imaging equipment and acquisition sequences are used (Galbraith et al. 2002).

Quantitative analysis offers more accurate physiological and pathophysiological insights while also addressing reproducibility issues through standardisation, thereby facilitating multi-centre clinical trials and longitudinal studies. However, the accuracy of AIF estimation and the selection of an appropriate model remain critical challenges, as suboptimal choices can lead to distorted parameter estimates (F. Khalifa et al. 2014). Table 4.4 provides an overview of key parameters used in quantitative analysis, their interpretations, and the models in which they appear.

Table 4.4: Quantitative DCE-MRI parameters.

Parameter	**Description**	**Model**	**Units**
K^{trans}	Volume transfer coefficient between plasma and EES	TK,ETK,2CXM	min^{-1}
k_{ep}	Rate constant between plasma and EES, K^{trans}/v_e	TK,ETK,2CXM	min^{-1}
v_p	Plasma volume	ETK,2CXM	Arbitrary Units
v_e	EES volume	TK,ETK,2CXM	Arbitrary Units
F_b	Blood flow	2CXM	mL/mL/min
F_p	Plasma flow	2CXM	mL/mL/min
PS	Permeability (P) surface area (S) product	2CXM	mL/mL/min
τ_i	Mean lifetime of water in EIS	SSM	sec

4.3 Common Goal in DSC and DCE Quantitative Analysis

Although DSC- and DCE-MRI utilise different acquisition protocols, they share a common quantitative goal: to characterise tissue perfusion and vascular properties by analysing the dynamics of CA distribution using the same underlying kinetic model:

$$C_t(t) = f \cdot C_p(t) \otimes R(t) \tag{4.10}$$

Once the tissue concentration time curve, $C_t(t)$, and the plasma concentration time curve, $C_p(t)$, are accurately estimated, various PK models, such as the ETK model, can be applied to both DSC and DCE concentrations to extract physiological parameters (Rotkopf et al. 2022).

In addition, studies have demonstrated correlations between perfusion parameters derived from DSC-MRI and those obtained from DCE-MRI. For instance, significant associations have been reported between relative cerebral blood volume ($rCBV$) in DSC-MRI and both the volume transfer constant (K^{trans}) and plasma volume fraction (v_p) in DCE-MRI, suggesting that these parameters may reflect similar underlying physiological processes (Artzi et al. 2015; Sanders et al. 2021).

Therefore, by leveraging appropriate PK modelling techniques on the reconstructed $C_t(t)$, both DSC- and DCE-MRI can provide complementary insights into tissue perfusion and vascular characteristics, enhancing diagnostic accuracy and treatment monitoring in various clinical and research settings.

4.4 Conclusion

This chapter provides a systematic overview of semi-quantitative and quantitative analytical frameworks for DSC- and DCE-MRI. Once tissue CA concentration is obtained, quantitative PK models can be applied to estimate perfusion parameters, regardless of the imaging protocol used. While the two techniques differ in acquisition protocols and signal mechanisms, they share a common analytical foundation. Key distinctions, however, emerge in their clinical applications: DSC-MRI offers rapid quantification of hemodynamic parameters such as cerebral blood flow and volume, whereas DCE-MRI enables characterisation of tissue perfusion, microvascular permeability, and extracellular volume fraction. Each technique presents unique clinical advantages, specifically, DSC is prioritised for its efficiency in capturing haemodynamic changes, while DCE is preferred for its sensitivity to vascular permeability and tissue structure.

Furthermore, emerging protocols integrating both bolus-tracking approaches hold significant promise for advancing multi-parametric tissue characterisation in oncology and cerebrovascular disease management. The synergistic application of these complementary techniques may enhance diagnostic specificity and therapeutic

monitoring capabilities in clinical practice.

University College Cork, Ireland
Coláiste na hOllscoile Corcaigh

CORA
Cork Open Research Archive
Cartlann Taighde Oscailte Chorcaí

Hu, Y. 2025. A statistical re-examination of the spoiled gradient recall echo equation in the analysis of data from DSC and DCE MR imaging procedures. PhD Thesis, University College Cork.

Please note that Chapter 5 (pp. 131-164) is unavailable due to a request by the author.

CORA Cork Open Research Archive http://cora.ucc.ie

Chapter 6

Discussion and Future Work

This thesis began with an overview of MRI development, introducing the mechanism of MR and presenting a PK analysis framework that spans from signal conversion to the estimation of perfusion parameters. It further discussed the clinical relevance of these parameters, particularly in precise tumour identification and assessment of treatment efficacy using both DSC- and DCE-MRI techniques. A novel signal reconstruction method, a two-parameter model, was proposed, which demonstrates improved reconstruction of relative signal intensity and yields more accurate parameter estimates in different types of tissues during the signal reconstruction process. Furthermore, when combined with the ETK model, the proposed direct optimisation of the ETK model yields distinct perfusion parameter estimates, particularly in pathological regions and areas with abnormal signal profiles. These findings suggest that the accuracy of signal intensity reconstruction directly influences the estimation of physiological and pathological metrics.

The chapter 2 provides an overview of the development of MR scanners and the mechanism of MRI, including key parameters for acquiring the spoiled-GRE sequences. The chapter explains the reconstruction process of MR signal intensity from k-space to the image domain, and introduces various perfusion MRI techniques along with commonly used CAs. It highlights the critical role of MRI in both clinical and research settings, while also emphasising the potential risks associated with its use in patients.

The chapter 3 reviews existing signal conversion approaches in DSC- and DCE-MRI, summarising their advantages and limitations. It highlights common reconstruction artifacts associated with the traditional techniques and emphasises the importance of T_{10} in the DSC-MRI signal conversion process, particularly in the CSF region. It also reveals discrepancies in the SSS and CM regions when conventional methods are used to reconstruct concentration in DCE-MRI. To address these challenges, a novel two-parameter method was proposed. Through identifiability analysis and numerical simulations, the method is shown to more accurately reconstruct signal intensity and reliably estimate baseline relaxation time rate-related parameters (α) along with the concentration scaling factor (β).

The chapter 4 provides a comprehensive review of widely used PK models. Begins by outlining three key assumptions commonly made in DSC-MRI analysis, including negligible T_1 shortening effects due to CA extravasation, absence of CA recirculation, and no delays or dispersion in the AIF. The chapter then discusses correction strategies applied when these assumptions are violated. The DCE-MRI section introduces clinically established models such as the TK and ETK mod-

els. When standard assumptions, such as uniform CA distribution, are violated, alternative models, like the DP model, become more appropriate. Furthermore, when water exchange is finite, the SSM offers a better representation of tissue kinetics. This chapter also summarises the common objective of quantitative analysis in both DSC- and DCE-MRI, highlighting that once the concentration is reconstructed, PK models such as the ETK model can be applied to either MR protocol.

The chapter 5 applies the proposed direct optimisation of the ETK model to clinical data and compares its performance with conventional approaches. By evaluating the reconstructed relative signal intensity, $S(t)/S_0$, and the associated conversion parameters α and β, the results demonstrate that the direct optimisation of the ETK model more accurately recovers both signal intensity and conversion parameter estimates across different anatomical tissues. Moreover, comparisons between perfusion parameters reveal that the accuracy of reconstructed signal intensities directly influences the estimation of physiological and pathological metrics. Consequently, the improved accuracy achieved by the direct optimisation of the ETK model leads to more reliable concentration estimates and potentially more robust perfusion quantification.

6.1 Discussion

This study reveals critical limitations of conventional signal conversion techniques in signal reconstruction and accurately quantifying CA concentrations, particularly

within CSF and CM regions of the human brain. In contrast, the proposed direct optimisation of the ETK model demonstrates significantly improved accuracy across representative ROIs in both DSC- and DCE-MRI frameworks. Notably, our method highlights that the native longitudinal relaxation time also plays a significant role in the DSC-MRI conversion process. Moreover, this approach eliminates the need for pre-scanning to estimate baseline longitudinal relaxation time, a requirement that restricts the clinical practicality of the MFA method. Additionally, unlike the LL technique, which necessitates breath-holding, our approach exhibits broad applicability to diverse anatomical regions without requiring respiratory coordination, a feature particularly advantageous in pediatric or uncooperative patient populations. Furthermore, the comparison of perfusion parameters highlights that the accuracy of signal reconstruction affects the estimation of perfusion metrics, particularly in tumour regions and areas with abnormal signal profiles.

Despite the demonstrated improvements, this thesis has two limitations that warrant further investigation. First, while the proposed direct optimisation of the ETK model achieves robust performance in regional comparisons, its generalisability to voxel-level analyses across whole-brain or multi-organ applications remains unvalidated. Second, the method's foundational assumption of a linear relationship between CA concentration $C_t(t)$ and relaxation rates ($R_2^*(t)$ and $R_1(t)$) may fail in scenarios involving high concentrations or finite water exchange. In these situations, it is necessary to explore alternative models or apply correction strategies to address potential nonlinear effects.

6.2 Future Work

To address the above limitations, three targeted directions are proposed: (1) voxel-level validation: the method's accuracy will be evaluated using more patients from the ACRIN-6684 clinical dataset, comparing voxel-wise signal reconstructions between the direct optimisation of the ETK model and conventional techniques; (2) nonlinear relationship modelling: when the linear concentration and relaxivities assumption is violated, additional corrections will be incorporated to ensure accurate signal modelling; and (3) multi-organ generalisability: while the current analysis focuses on the human brain, future studies will extend the validation to additional anatomical regions such as the heart, prostate, and soft tissue sarcomas.

In addition, the direct optimisation of the ETK model methodology developed in this thesis will be implemented as a publicly available software package on the Comprehensive R Archive Network (CRAN[1]). This package will offer a more user-friendly interface, facilitating broader accessibility and application in both research and clinical settings.

Moreover, some non-parametric PK models, such as mixture analysis and non-parametric residue mapping (NPRM) techniques, have been validated in other DCE-MRI studies for recovering localised kinetic information. As part of future investigations, the proposed direct optimisation of the ETK model will be combined with the NPRM model on the ACRIN-6684 dataset to generate kinetic parametric maps.

[1] `https://cran.r-project.org/`

References

Amano, Yasuo, Morimasa Takayama and Shinichiro Kumita (2009). 'Contrast-enhanced myocardial T1-weighted scout (Look–Locker) imaging for the detection of myocardial damages in hypertrophic cardiomyopathy'. In: *Journal of Magnetic Resonance Imaging: An Official Journal of the International Society for Magnetic Resonance in Medicine* 30.4, pp. 778–784.

Antoch, Gerald and Andreas Bockisch (2009). 'Combined PET/MRI: a new dimension in whole-body oncology imaging?' In: *European journal of nuclear medicine and molecular imaging* 36, pp. 113–120.

Aronen, Hannu J et al. (2000). 'High microvascular blood volume is associated with high glucose uptake and tumor angiogenesis in human gliomas'. In: *Clinical Cancer Research* 6.6, pp. 2189–2200.

Artzi, Moran et al. (2015). 'Human cerebral blood volume measurements using dynamic contrast enhancement in comparison to dynamic susceptibility contrast MRI'. In: *Neuroradiology* 57, pp. 671–678.

Barbier, EL (2013). 'T2-* weighted perfusion MRI'. In: *Diagnostic and Interventional Imaging* 94.12, pp. 1205–1209.

Benner, Thomas et al. (1997). 'Accuracy of gamma-variate fits to concentration-time curves from dynamic susceptibility-contrast enhanced MRI: influence of time resolution, maximal signal drop and signal-to-noise'. In: *Magnetic resonance imaging* 15.3, pp. 307–317.

Bercovich, Eyal and Marcia C Javitt (2018). 'Medical imaging: from roentgen to the digital revolution, and beyond'. In: *Rambam Maimonides medical journal* 9.4.

Berger, Abi (2002). 'How does it work?: Magnetic resonance imaging'. In: *BMJ: British Medical Journal* 324.7328, p. 35.

Bernstein, Jonathan M, Jarrod J Homer and Catharine M West (2014). 'Dynamic contrast-enhanced magnetic resonance imaging biomarkers in head and neck cancer: potential to guide treatment? A systematic review'. In: *Oral oncology* 50.10, pp. 963–970.

Bian, Yitong et al. (2020). 'Clinical applications of DSC-MRI parameters assess angiogenesis and differentiate malignant from benign soft tissue tumors in limbs'. In: *Academic Radiology* 27.3, pp. 354–360.

Bidgood Jr, W Dean et al. (1997). 'Understanding and using DICOM, the data interchange standard for biomedical imaging'. In: *Journal of the American Medical Informatics Association* 4.3, pp. 199–212.

Bloch, Felix and WWPM Hansen (1946). 'W., Packard, M. The nuclear induction experiment'. In: *Physical review* 70.7-8, pp. 474–485.

Bojorquez, Jorge Zavala et al. (2017). 'What are normal relaxation times of tissues at 3 T?' In: *Magnetic resonance imaging* 35, pp. 69–80.

Boxerman, Jerrold L, Bruce R Rosen and Robert M Weisskoff (1997). 'Signal-to-noise analysis of cerebral blood volume maps from dynamic NMR imaging studies'. In: *Journal of Magnetic Resonance Imaging* 7.3, pp. 528–537.

Boxerman, JL et al. (2012). 'The role of preload and leakage correction in gadolinium-based cerebral blood volume estimation determined by comparison with MION as a criterion standard'. In: *American journal of neuroradiology* 33.6, pp. 1081–1087.

Boyle, Gerard E et al. (2006). 'An interactive taxonomy of MR imaging sequences'. In: *Radiographics* 26.6, e24–e24.

Bright, Anne (2011). *Planning and Positioning in MRI-E-Book*. Elsevier Health Sciences.

Brix, Gunnar et al. (1991). 'Pharmacokinetic parameters in CNS Gd-DTPA enhanced MR imaging'. In: *Journal of computer assisted tomography* 15.4, pp. 621–628.

Brookes, JA et al. (1996). 'Measurement of spin-lattice relaxation times with FLASH for dynamic MRI of the breast'. In: *The British journal of radiology* 69.819, pp. 206–214.

Buckley, David L (2002). 'Uncertainty in the analysis of tracer kinetics using dynamic contrast-enhanced T1-weighted MRI'. In: *Magnetic Resonance in Medicine: An Official Journal of the International Society for Magnetic Resonance in Medicine* 47.3, pp. 601–606.

Buckley, David L and Geoffrey JM Parker (2005). *Measuring contrast agent concentration in T1-weighted dynamic contrast-enhanced MRI*. Springer, pp. 69–79.

Buxton, Richard B et al. (1987). 'Contrast in rapid MR imaging: T1-and T2-weighted imaging'. In: *J Comput Assist Tomogr* 11.1, pp. 7–16.

Calamante, F, DG Gadian and A Connelly (2002). 'Quantification of perfusion using bolus tracking magnetic resonance imaging in stroke: assumptions, limitations, and potential implications for clinical use'. In: *Stroke* 33.4, pp. 1146–1151.

Calamante, Fernando (2005). 'Bolus dispersion issues related to the quantification of perfusion MRI data'. In: *Journal of Magnetic Resonance Imaging: An Official Journal of the International Society for Magnetic Resonance in Medicine* 22.6, pp. 718–722.

— (2010). 'Perfusion MRI using dynamic-susceptibility contrast MRI: quantification issues in patient studies'. In: *Topics in magnetic resonance imaging* 21.2, pp. 75–85.

— (2013). 'Arterial input function in perfusion MRI: a comprehensive review'. In: *Progress in nuclear magnetic resonance spectroscopy* 74, pp. 1–32.

Calamante, Fernando, Alan Connelly and Matthias JP van Osch (2009). 'Nonlinear ΔR effects in perfusion quantification using bolus-tracking MRI'. In: *Magnetic Resonance in Medicine: An Official Journal of the International Society for Magnetic Resonance in Medicine* 61.2, pp. 486–492.

Calamante, Fernando, David G Gadian and Alan Connelly (2000). 'Delay and dispersion effects in dynamic susceptibility contrast MRI: simulations using singular value decomposition'. In: *Magnetic Resonance in Medicine: An Official Journal of the International Society for Magnetic Resonance in Medicine* 44.3, pp. 466–473.

Calamante, Fernando, Evert-jan PA Vonken and Matthias JP van Osch (2007). 'Contrast agent concentration measurements affecting quantification of bolus-tracking perfusion MRI'. In: *Magnetic Resonance in Medicine: An Official Journal of the International Society for Magnetic Resonance in Medicine* 58.3, pp. 544–553.

Calamante, Fernando et al. (2006). 'Bolus delay and dispersion in perfusion MRI: implications for tissue predictor models in stroke'. In: *Magnetic Resonance*

in Medicine: An Official Journal of the International Society for Magnetic Resonance in Medicine 55.5, pp. 1180–1185.

Cárdenas-Rodríguez, J et al. (2016). 'The basic principles of dynamic contrast-enhanced magnetic resonance imaging'. In: *MR and CT Perfusion and Pharmacokinetic Imaging. Clinical Applications and Theory; Bammer, R., Ed*, pp. 332–347.

Carr, Herman Y (1953). 'Free Precession Techniques in Nuclear Magnetic Resonance.' In: *Ph. D. Thesis*.

Cecil, Kim M (2013). 'Proton magnetic resonance spectroscopy: technique for the neuroradiologist'. In: *Neuroimaging Clinics of North America* 23.3, p. 381.

Chavhan, Govind B et al. (2008). 'Steady-state MR imaging sequences: physics, classification, and clinical applications'. In: *Radiographics* 28.4, pp. 1147–1160.

Chavhan, Govind B et al. (2009). 'Principles, techniques, and applications of T2*-based MR imaging and its special applications'. In: *Radiographics* 29.5, pp. 1433–1449.

Cheng, Hai-Ling Margaret and Graham A Wright (2006). 'Rapid high-resolution T1 mapping by variable flip angles: accurate and precise measurements in the presence of radiofrequency field inhomogeneity'. In: *Magnetic Resonance in Medicine: An Official Journal of the International Society for Magnetic Resonance in Medicine* 55.3, pp. 566–574.

Cheong, Benjamin YC et al. (2022). 'Gadolinium-based contrast agents: updates and answers to typical questions regarding gadolinium use'. In: *Texas Heart Institute Journal* 49.3, e217680.

Chow, Lucy and Bo Li (2022). *Absolute Breast Imaging: Multimodality Cases for the Core Exam*. Springer Nature Switzerland. ISBN: 978-3-031-08273-3. URL: https://doi.org/10.1007/978-3-031-08274-0.

Clare, Stuart and Peter Jezzard (2001). 'Rapid T1 mapping using multislice echo planar imaging'. In: *Magnetic Resonance in Medicine: An Official Journal of the International Society for Magnetic Resonance in Medicine* 45.4, pp. 630–634.

Clarke, A Grey (1944). 'The anatomy of the meninges'. In: *Postgraduate Medical Journal* 20.220, p. 74.

Cobelli, Claudio, Gianna Toffolo and David M Foster (1992). 'Tracer-to-tracee ratio for analysis of stable isotope tracer data: link with radioactive kinetic formalism'. In: *American Journal of Physiology-Endocrinology and Metabolism* 262.6, E968–E975.

Creager, Mark, Joshua A Beckman and Joseph Loscalzo (2012). *Vascular Medicine: A Companion to Braunwald's Heart Disease: Expert Consult-Online and Print*. Elsevier Health Sciences.

Damadian, Raymond (1971). 'Tumor detection by nuclear magnetic resonance'. In: *Science* 171.3976, pp. 1151–1153.

Dance, D.R. and International Atomic Energy Agency (2014). *Diagnostic Radiology Physics: A Handbook for Teachers and Students*. STI/PUB. International Atomic Energy Agency. ISBN: 9789201310101. URL: https://books.google.ie/books?id=9iiKmwEACAAJ.

Davson, Hugh, Keasley Welch and Malcolm Beverley Segal (1987). 'Physiology and pathophysiology of the cerebrospinal fluid'. In: *(No Title)*.

Deibler, AR et al. (2008). 'Arterial spin-labeling in routine clinical practice, part 1: technique and artifacts'. In: *American Journal of Neuroradiology* 29.7, pp. 1228–1234.

Detre, John A et al. (1992). 'Perfusion imaging'. In: *Magnetic resonance in medicine* 23.1, pp. 37–45.

Donahue, Kathleen M et al. (2000). 'Utility of simultaneously acquired gradient-echo and spin-echo cerebral blood volume and morphology maps in brain tumor patients'. In: *Magnetic resonance in medicine* 43.6, pp. 845–853.

Donaldson, Stephanie B et al. (2010). 'A comparison of tracer kinetic models for T1-weighted dynamic contrast-enhanced MRI: Application in carcinoma of the cervix'. In: *Magnetic Resonance in Medicine* 63.3, pp. 691–700.

Englund, Erin K et al. (2013). 'Combined measurement of perfusion, venous oxygen saturation, and skeletal muscle T2* during reactive hyperemia in the leg'. In: *Journal of Cardiovascular Magnetic Resonance* 15.1, p. 70.

Erlemann, Rainer et al. (1989). 'Musculoskeletal neoplasms: static and dynamic Gd-DTPA–enhanced MR imaging.' In: *Radiology* 171.3, pp. 767–773.

Ernst, Richard R and Weston A Anderson (1966). 'Application of Fourier transform spectroscopy to magnetic resonance'. In: *Review of Scientific Instruments* 37.1, pp. 93–102.

Essig, Marco et al. (2013). 'Perfusion MRI: the five most frequently asked technical questions'. In: *American journal of roentgenology* 200.1, pp. 24–34.

Essock-Burns, Emma et al. (2013). 'Comparison of DSC-MRI post-processing techniques in predicting microvascular histopathology in patients newly diagnosed with GBM'. In: *Journal of Magnetic Resonance Imaging* 38.2, pp. 388–400.

Ferré, Jean-Christophe, Mark S Shiroishi and Meng Law (2012). 'Advanced techniques using contrast media in neuroimaging'. In: *Magnetic resonance imaging clinics of North America* 20.4, pp. 699–713.

Fram, Evan K et al. (1987). 'Rapid calculation of T1 using variable flip angle gradient refocused imaging'. In: *Magnetic resonance imaging* 5.3, pp. 201–208.

Fukatsu, Hiroshi (2003). '3T MR for clinical use: update'. In: *Magnetic Resonance in Medical Sciences* 2.1, pp. 37–45.

Gadian, DG et al. (1985). 'Gadolinium-DTPA as a contrast agent in MR imaging—theoretical projections and practical observations'. In: *Journal of computer assisted tomography* 9.2, pp. 242–251.

Galbraith, Susan M et al. (2002). 'Reproducibility of dynamic contrast-enhanced MRI in human muscle and tumours: comparison of quantitative and semi-quantitative analysis'. In: *NMR in Biomedicine: An International Journal Devoted to the Development and Application of Magnetic Resonance In Vivo* 15.2, pp. 132–142.

Gallagher, Thomas A, Alexander J Nemeth and Lotfi Hacein-Bey (2008). 'An introduction to the Fourier transform: relationship to MRI'. In: *American journal of roentgenology* 190.5, pp. 1396–1405.

Gerstner, Elizabeth R et al. (2016). 'ACRIN 6684: assessment of tumor hypoxia in newly diagnosed glioblastoma using 18F-FMISO PET and MRI'. In: *Clinical Cancer Research* 22.20, pp. 5079–5086.

Gold, Garry E et al. (2004). 'Musculoskeletal MRI at 3.0 T: relaxation times and image contrast'. In: *American Journal of Roentgenology* 183.2, pp. 343–351.

Gordon, Yaron et al. (2014). 'Dynamic contrast-enhanced magnetic resonance imaging: fundamentals and application to the evaluation of the peripheral perfusion'. In: *Cardiovascular diagnosis and therapy* 4.2, p. 147.

Gowland, P et al. (1992). 'Dynamic studies of gadolinium uptake in brain tumors using inversion-recovery echo-planar imaging'. In: *Magnetic resonance in medicine* 26.2, pp. 241–258.

Grant, Andrea et al. (2020). '10.5 T MRI static field effects on human cognitive, vestibular, and physiological function'. In: *Magnetic resonance imaging* 73, pp. 163–176.

Graves, Martin John (2022). '3 T: the good, the bad and the ugly'. In: *The British Journal of Radiology* 95.1130, p. 20210708.

Grøvik, Endre, Atle Bjørnerud and Kyrre Eeg Emblem (2020). 'Dynamic Susceptibility Contrast MRI: Basic Physics, Pulse Sequences, and Modeling'. In: *Advances in Magnetic Resonance Technology and Applications*. Vol. 1. Elsevier, pp. 345–367.

Grøvik, Endre et al. (2014). 'Split dynamic MRI: Single bolus high spatial–temporal resolution and multi contrast evaluation of breast lesions'. In: *Journal of Magnetic Resonance Imaging* 39.3, pp. 673–682.

Grøvik, Endre et al. (2017). 'Dynamic multi-echo DCE-and DSC-MRI in rectal cancer: Low primary tumor Ktrans and peak are significantly associated with lymph node metastasis'. In: *Journal of Magnetic Resonance Imaging* 46.1, pp. 194–206.

Guo, Jun-Yu et al. (2009). 'Dynamic contrast-enhanced magnetic resonance imaging parameters independent of baseline T10 values'. In: *Magnetic resonance imaging* 27.9, pp. 1208–1215.

Hahn, Erwin L (1950a). 'Nuclear induction due to free Larmor precession'. In: *Physical Review* 77.2, p. 297.

Hahn, Erwin L (1950b). 'Spin echoes'. In: *Physical review* 80.4, p. 580.

Haidekker, Mark A (2013). *Medical imaging technology.*

Haller, Sven et al. (2013). 'Acute caffeine administration impact on working memory-related brain activation and functional connectivity in the elderly: a BOLD and perfusion MRI study'. In: *Neuroscience* 250, pp. 364–371.

Hansen, Michael S and Peter Kellman (2015). 'Image reconstruction: an overview for clinicians'. In: *Journal of Magnetic Resonance Imaging* 41.3, pp. 573–585.

Hargreaves, Brian (2012). 'Rapid gradient-echo imaging'. In: *Journal of Magnetic Resonance Imaging* 36.6, pp. 1300–1313.

Hendrick, RE et al. (2005). 'Glossary of MR terms'. In: *American College of Radiology.*

Heye, Tobias et al. (2014). 'Impact of precontrast T10 relaxation times on dynamic contrast-enhanced MRI pharmacokinetic parameters: T10 mapping versus a fixed T10 reference value'. In: *Journal of Magnetic Resonance Imaging* 39.5, pp. 1136–1145.

Hu, Zhenghui et al. (2021). 'A Novel Statistical Optimization Algorithm for Estimating Perfusion Curves in Susceptibility Contrast-Enhanced MRI'. In: *Frontiers in Neuroscience* 15, p. 713893.

Huang, Wei et al. (2008). 'The magnetic resonance shutter speed discriminates vascular properties of malignant and benign breast tumors in vivo'. In: *Proceedings of the National Academy of Sciences* 105.46, pp. 17943–17948.

Hunter, George J et al. (1998). 'Dynamic T1-weighted magnetic resonance imaging and positron emission tomography in patients with lung cancer: correlating vascular physiology with glucose metabolism.' In: *Clinical cancer research: an official journal of the American Association for Cancer Research* 4.4, pp. 949–955.

Ibrahim, Michael A, Bita Hazhirkarzar and Arthur B Dublin (2023). *Gadolinium Magnetic Resonance Imaging*.

Isebaert, Sofie et al. (2012). 'Evaluation of semi-quantitative dynamic contrast-enhanced MRI parameters for prostate cancer in correlation to whole-mount histopathology'. In: *European journal of radiology* 81.3, e217–e222.

Jadvar, Hossein and Patrick M Colletti (2014). 'Competitive advantage of PET/MRI'. In: *European journal of radiology* 83.1, pp. 84–94.

Jahng, Geon-Ho et al. (2014). 'Perfusion magnetic resonance imaging: a comprehensive update on principles and techniques'. In: *Korean journal of radiology* 15.5, pp. 554–577.

Jerosch-Herold, Michael et al. (1998). 'Magnetic resonance quantification of the myocardial perfusion reserve with a Fermi function model for constrained deconvolution'. In: *Medical physics* 25.1, pp. 73–84.

Johnson, John A and Theodore A Wilson (1966). 'A model for capillary exchange'. In: *American Journal of Physiology-Legacy Content* 210.6, pp. 1299–1303.

Johnson, Kevin M et al. (2000). 'Intravascular susceptibility agent effects on tissue transverse relaxation rates in vivo'. In: *Magnetic Resonance in Medicine: An Official Journal of the International Society for Magnetic Resonance in Medicine* 44.6, pp. 909–914.

Jornada, Tiago da Silva, Camila Hitomi Murata and Regina Bitelli Medeiros (2016). 'Influence of partial k-space filling on the quality of magnetic resonance images'. In: *Radiologia Brasileira* 49, pp. 158–164.

Kabasawa, Hiroyuki (2022). 'MR imaging in the 21st century: technical innovation over the first two decades'. In: *Magnetic resonance in medical sciences* 21.1, pp. 71–82.

Kahn, Charles E et al. (2007). 'DICOM and radiology: past, present, and future'. In: *Journal of the American College of Radiology* 4.9, pp. 652–657.

Kang, Seong-Hyeon and Youngjin Lee (2024). 'Motion Artifact Reduction Using U-Net Model with Three-Dimensional Simulation-Based Datasets for Brain Magnetic Resonance Images'. In: *Bioengineering* 11.3, p. 227.

Kershaw, Lucy E and Hai-Ling Margaret Cheng (2010). 'Temporal resolution and SNR requirements for accurate DCE-MRI data analysis using the AATH model'. In: *Magnetic Resonance in Medicine* 64.6, pp. 1772–1780.

Khalifa, Fahmi et al. (2014). 'Models and methods for analyzing DCE-MRI: A review'. In: *Medical physics* 41.12, p. 124301.

Khalifa, Mohamed and Mona Albadawy (2024). 'AI in diagnostic imaging: Revolutionising accuracy and efficiency'. In: *Computer Methods and Programs in Biomedicine Update*, p. 100146.

Kjølby, Birgitte Fuglsang, Leif Østergaard and Valerij G Kiselev (2006). 'Theoretical model of intravascular paramagnetic tracers effect on tissue relaxation'. In: *Magnetic Resonance in Medicine: An Official Journal of the International Society for Magnetic Resonance in Medicine* 56.1, pp. 187–197.

Krupa, Katarzyna and Monika Bekiesińska-Figatowska (2015). 'Artifacts in magnetic resonance imaging'. In: *Polish journal of radiology* 80, p. 93.

Kshatri, Sapna Singh and Deepak Singh (2023). 'Convolutional neural network in medical image analysis: a review'. In: *Archives of Computational Methods in Engineering* 30.4, pp. 2793–2810.

Landis, Charles S et al. (2000). 'Determination of the MRI contrast agent concentration time course in vivo following bolus injection: effect of equilibrium transcytolemmal water exchange'. In: *Magnetic resonance in medicine* 44.4, pp. 563–574.

Larmor, Joseph (1897). 'LXIII. On the theory of the magnetic influence on spectra; and on the radiation from moving ions'. In: *The London, Edinburgh, and Dublin Philosophical Magazine and Journal of Science* 44.271, pp. 503–512.

Larsson, HBW et al. (1990). 'Quantitation of blood-brain barrier defect by magnetic resonance imaging and gadolinium-DTPA in patients with multiple sclerosis and brain tumors'. In: *Magnetic Resonance in Medicine* 16.1, pp. 117–131.

Lauterbur, Paul C (1973). 'Image formation by induced local interactions: examples employing nuclear magnetic resonance'. In: *nature* 242.5394, pp. 190–191.

Li, Xia et al. (2012). 'Statistical comparison of dynamic contrast-enhanced MRI pharmacokinetic models in human breast cancer'. In: *Magnetic resonance in medicine* 68.1, pp. 261–271.

Li, Xiangrui et al. (2016). 'The first step for neuroimaging data analysis: DICOM to NIfTI conversion'. In: *Journal of neuroscience methods* 264, pp. 47–56.

Li, Xin, William D Rooney and Charles S Springer Jr (2005). 'A unified magnetic resonance imaging pharmacokinetic theory: intravascular and extracellular contrast reagents'. In: *Magnetic Resonance in Medicine* 54.6, pp. 1351–1359.

Lind, Emelie et al. (2017). 'Assessment of MRI contrast agent concentration by quantitative susceptibility mapping (QSM): application to estimation of cerebral blood volume during steady state'. In: *Magnetic Resonance Materials in Physics, Biology and Medicine* 30.6, pp. 555–566.

Lohrke, Jessica et al. (2016). '25 years of contrast-enhanced MRI: developments, current challenges and future perspectives'. In: *Advances in therapy* 33, pp. 1–28.

Look, David C and Donald R Locker (1970). 'Time saving in measurement of NMR and EPR relaxation times'. In: *Review of scientific instruments* 41.2, pp. 250–251.

MacWilliams, Bryon (2003). 'Russian claims first in magnetic imaging.' In: *Nature* 426.6965, pp. 375–376.

Mansfield, Peter (1977). 'Multi-planar image formation using NMR spin echoes'. In: *Journal of Physics C: Solid State Physics* 10.3, p. L55.

Markl, Michael and Jochen Leupold (2012). 'Gradient echo imaging'. In: *Journal of Magnetic Resonance Imaging* 35.6, pp. 1274–1289.

Martino, Francesca et al. (2021). 'Gadolinium-based contrast media nephrotoxicity in kidney impairment: the physio-pathological conditions for the perfect murder'. In: *Journal of Clinical Medicine* 10.2, p. 271.

McGarry, Sean D et al. (2022). 'Multi-Site Concordance of Diffusion-Weighted Imaging Quantification for Assessing Prostate Cancer Aggressiveness'. In: *Journal of Magnetic Resonance Imaging* 55.6, pp. 1745–1758.

McLeod, Shaunna M and Thomas J Meade (2021). 'Magnetic Resonance Theranostics: An Overview of Gadolinium (III)-Based Strategies and Magnetic Particle Imaging'. In: *Metal Ions in Bio-Imaging Techniques*, p. 347.

Moratal, David et al. (2008). 'k-Space tutorial: an MRI educational tool for a better understanding of k-space'. In: *Biomedical imaging and intervention journal* 4.1.

Moser, Ewald et al. (2009). 'Magnetic resonance imaging methodology'. In: *European journal of nuclear medicine and molecular imaging* 36, pp. 30–41.

Mouridsen, Kim et al. (2006). 'Bayesian estimation of cerebral perfusion using a physiological model of microvasculature'. In: *Neuroimage* 33.2, pp. 570–579.

Noebauer-Huhmann, Iris M et al. (2010). 'Gadolinium-based magnetic resonance contrast agents at 7 Tesla: in vitro T: 1: relaxivities in human blood plasma'. In: *Investigative radiology* 45.9, pp. 554–558.

O'connor, JPB et al. (2011). 'Dynamic contrast-enhanced imaging techniques: CT and MRI'. In: *The British journal of radiology* 84.special_issue_2, S112–S120.

Odeblad, Erik and Gunnar Lindström (1955). 'Some preliminary observations on the proton magnetic resonance in biologic samples'. In: *Acta Radiologica* 6, pp. 469–476.

Ogawa, Seiji et al. (1990). 'Brain magnetic resonance imaging with contrast dependent on blood oxygenation.' In: *proceedings of the National Academy of Sciences* 87.24, pp. 9868–9872.

Ordidge, RJ et al. (1990). 'High-speed multislice T1 mapping using inversion-recovery echo-planar imaging'. In: *Magnetic resonance in medicine* 16.2, pp. 238–245.

Orsingher, Laura, Silvia Piccinini and Girolamo Crisi (2014). 'Differences in dynamic susceptibility contrast MR perfusion maps generated by different methods implemented in commercial software'. In: *Journal of computer assisted tomography* 38.5, pp. 647–654.

Ou, Xiangyu et al. (2021). 'Recent development in x-ray imaging technology: Future and challenges'. In: *Research*.

Paldino, Michael J and Daniel P Barboriak (2009). 'Fundamentals of quantitative dynamic contrast-enhanced MR imaging'. In: *Magnetic resonance imaging clinics of North America* 17.2, pp. 277–289.

Parker, Geoff JM et al. (2006). 'Experimentally-derived functional form for a population-averaged high-temporal-resolution arterial input function for dynamic contrast-enhanced MRI'. In: *Magnetic Resonance in Medicine: An Official Journal of the International Society for Magnetic Resonance in Medicine* 56.5, pp. 993–1000.

Paulson, Eric S, Douglas E Prah and Kathleen M Schmainda (2016). 'Spiral perfusion imaging with consecutive echoes (SPICE™) for the simultaneous mapping of DSC-and DCE-MRI parameters in brain tumor patients: theory and initial feasibility'. In: *Tomography* 2.4, p. 295.

Paulson, Eric S and Kathleen M Schmainda (2008). 'Comparison of dynamic susceptibility-weighted contrast-enhanced MR methods: recommendations for measuring relative cerebral blood volume in brain tumors'. In: *Radiology* 249.2, pp. 601–613.

Perthen, Joanna E et al. (2002). 'Is quantification of bolus tracking MRI reliable without deconvolution?' In: *Magnetic Resonance in Medicine: An Official Journal of the International Society for Magnetic Resonance in Medicine* 47.1, pp. 61–67.

Petrella, Jeffrey R and James M Provenzale (2000). 'MR perfusion imaging of the brain: techniques and applications'. In: *American Journal of roentgenology* 175.1, pp. 207–219.

Pui, MH and EC Fok (1995). 'MR imaging of the brain: comparison of gradient-echo and spin-echo pulse sequences.' In: *AJR. American journal of roentgenology* 165.4, pp. 959–962.

Rempp, Katrin A et al. (1994). 'Quantification of regional cerebral blood flow and volume with dynamic susceptibility contrast-enhanced MR imaging.' In: *Radiology* 193.3, pp. 637–641.

Ridgway, John P (2010). 'Cardiovascular magnetic resonance physics for clinicians: part I'. In: *Journal of cardiovascular magnetic resonance* 12.1, p. 71.

— (2015). 'Gradient Echo Versus Spin Echo'. In: *Cardiovascular MR Manual*. Ed. by Sven Plein, John Greenwood and John P. Ridgway. Cham: Springer

International Publishing, pp. 91–95. ISBN: 978-3-319-20940-1. DOI: 10.1007/978-3-319-20940-1_11. URL: https://doi.org/10.1007/978-3-319-20940-1_11.

Rinck, Peter A (2019). *Magnetic resonance in medicine: a critical introduction*. BoD–Books on Demand.

Roberts, George W, Kenneth B Larson and Edmund E Spaeth (1973). 'The interpretation of mean transit time measurements for multiphase tissue systems'. In: *Journal of Theoretical Biology* 39.2, pp. 447–475.

Rohrer, Martin et al. (2005). 'Comparison of magnetic properties of MRI contrast media solutions at different magnetic field strengths'. In: *Investigative radiology* 40.11, pp. 715–724.

Rotkopf, Lukas T et al. (2022). 'Quantitative analysis of DCE and DSC-MRI: from kinetic modeling to deep learning'. In: *RöFo-Fortschritte auf dem Gebiet der Röntgenstrahlen und der bildgebenden Verfahren*. Vol. 194. 09. Georg Thieme Verlag KG, pp. 975–982.

Sanders, Jeremiah W et al. (2021). 'Synthetic generation of DSC-MRI-derived relative CBV maps from DCE MRI of brain tumors'. In: *Magnetic resonance in medicine* 85.1, pp. 469–479.

Sangren, WC and CW Sheppard (1953). 'A mathematical derivation of the exchange of a labeled substance between a liquid flowing in a vessel and

an external compartment'. In: *The bulletin of mathematical biophysics* 15, pp. 387–394.

Sawada, YASUFUMI, CLIFFORD S Patlak and RONALD G Blasberg (1989). 'Kinetic analysis of cerebrovascular transport based on indicator diffusion technique'. In: *American Journal of Physiology-Heart and Circulatory Physiology* 256.3, H794–H812.

Schmainda, Kathleen M et al. (2004). 'Characterization of a first-pass gradient-echo spin-echo method to predict brain tumor grade and angiogenesis'. In: *American Journal of Neuroradiology* 25.9, pp. 1524–1532.

Selvakumar, Ambika, Veena Noronha and Padmaja Minakshi Sundaram (2014). *Sankara Nethralaya's atlas of imaging in ophthalmology*. Jaypee Brothers Medical Publishers.

Shamir, Ittai and Yaniv Assaf (2025). 'Tutorial: a guide to diffusion MRI and structural connectomics'. In: *Nature Protocols* 20.2, pp. 317–335.

Shen, Yaqi et al. (2015). 'T1 relaxivities of gadolinium-based magnetic resonance contrast agents in human whole blood at 1.5, 3, and 7 T'. In: *Investigative radiology* 50.5, pp. 330–338.

Shiroishi, Mark S et al. (2015). 'Principles of T2*-weighted dynamic susceptibility contrast MRI technique in brain tumor imaging'. In: *Journal of magnetic resonance imaging* 41.2, pp. 296–313.

Simonsen, Claus Z et al. (1999). 'CBF and CBV measurements by USPIO bolus tracking: reproducibility and comparison with Gd-based values'. In: *Journal of Magnetic Resonance Imaging: An Official Journal of the International Society for Magnetic Resonance in Medicine* 9.2, pp. 342–347.

Sourbron, Steven et al. (2009). 'Quantification of cerebral blood flow, cerebral blood volume, and blood–brain-barrier leakage with DCE-MRI'. In: *Magnetic Resonance in Medicine: An Official Journal of the International Society for Magnetic Resonance in Medicine* 62.1, pp. 205–217.

Sourbron, Steven P and David L Buckley (2011). 'On the scope and interpretation of the Tofts models for DCE-MRI'. In: *Magnetic resonance in medicine* 66.3, pp. 735–745.

Stikov, Nikola et al. (2015). 'On the accuracy of T1 mapping: searching for common ground'. In: *Magnetic resonance in medicine* 73.2, pp. 514–522.

Symms, M et al. (2004). 'A review of structural magnetic resonance neuroimaging'. In: *Journal of Neurology, Neurosurgery & Psychiatry* 75.9, pp. 1235–1244.

Tadanki, Sasidhar (2018). 'Multiple resonant multiconductor transmission line resonator design using circulant block matrix algebra'. PhD thesis. PhD dissertation, Faculty of the Worcester Polytechnic Institute.

Tadimalla, Sirisha et al. (2022). 'Bias, repeatability and reproducibility of liver T1 mapping with variable flip angles'. In: *Journal of Magnetic Resonance Imaging* 56.4, pp. 1042–1052.

Tarroni, Giacomo et al. (2012). 'Myocardial perfusion: near-automated evaluation from contrast-enhanced MR images obtained at rest and during vasodilator stress'. In: *Radiology* 265.2, pp. 576–583.

Taylor, Andrew J et al. (2016). 'T1 mapping: basic techniques and clinical applications'. In: *JACC: Cardiovascular Imaging* 9.1, pp. 67–81.

Tircsó, Gyula et al. (2021). *Gadolinium (III)-Based Contrast Agents for Magnetic Resonance Imaging. A Re-Appraisal.*

Tofts, Paul S (1997). 'Modeling tracer kinetics in dynamic Gd-DTPA MR imaging'. In: *Journal of magnetic resonance imaging* 7.1, pp. 91–101.

— (2010). 'T1-weighted DCE imaging concepts: modelling, acquisition and analysis'. In: *signal* 500.450, p. 400.

Tofts, Paul S and Allan G Kermode (1991). 'Measurement of the blood-brain barrier permeability and leakage space using dynamic MR imaging. 1. Fundamental concepts'. In: *Magnetic resonance in medicine* 17.2, pp. 357–367.

Tubridy, N and CS McKinstry (2000). 'Neuroradiological history: Sir Joseph Larmor and the basis of MRI physics'. In: *Neuroradiology* 42, pp. 852–855.

Uematsu, Hidemasa et al. (2004). 'High field body MR imaging: preliminary experiences'. In: *Clinical imaging* 28.3, pp. 159–162.

Wang, Henry Z, Stephen J Riederer and James N Lee (1987). 'Optimizing the precision in T1 relaxation estimation using limited flip angles'. In: *Magnetic resonance in medicine* 5.5, pp. 399–416.

Welker, Kirk et al. (2015). 'ASFNR recommendations for clinical performance of MR dynamic susceptibility contrast perfusion imaging of the brain'. In: *American Journal of Neuroradiology* 36.6, E41–E51.

Westbrook, Catherine and John Talbot (2018). *MRI in Practice*. John Wiley & Sons.

Whitcher, Brandon and Volker J Schmid (2011). 'Quantitative analysis of dynamic contrast-enhanced and diffusion-weighted magnetic resonance imaging for oncology in R'. In: *Journal of Statistical Software* 44, pp. 1–29.

Willats, L, A Connelly and F Calamante (2008). 'Minimising the effects of bolus dispersion in bolus-tracking MRI'. In: *NMR in Biomedicine: An International Journal Devoted to the Development and Application of Magnetic Resonance In vivo* 21.10, pp. 1126–1137.

Willats, Lisa, Alan Connelly and Fernando Calamante (2006). 'Improved deconvolution of perfusion MRI data in the presence of bolus delay and dispersion'. In: *Magnetic Resonance in Medicine: An Official Journal of the International Society for Magnetic Resonance in Medicine* 56.1, pp. 146–156.

Willats, Lisa et al. (2011). 'Validating a local Arterial Input Function method for improved perfusion quantification in stroke'. In: *Journal of Cerebral Blood Flow & Metabolism* 31.11, pp. 2189–2198.

Wittsack, H-J et al. (2008). 'CT-perfusion imaging of the human brain: advanced deconvolution analysis using circulant singular value decomposition'. In: *Computerized Medical Imaging and Graphics* 32.1, pp. 67–77.

Yuan, Jing et al. (2012). 'Quantitative evaluation of dual-flip-angle T1 mapping on DCE-MRI kinetic parameter estimation in head and neck'. In: *Quantitative imaging in medicine and surgery* 2.4, p. 245.

Zhang, Xiaofei et al. (2013). 'In vivo blood T1 measurements at 1.5 T, 3 T, and 7 T'. In: *Magnetic resonance in medicine* 70.4, pp. 1082–1086.

Zhu, David C and Richard D Penn (2005). 'Full-brain T1 mapping through inversion recovery fast spin echo imaging with time-efficient slice ordering'. In: *Magnetic Resonance in Medicine: An Official Journal of the International Society for Magnetic Resonance in Medicine* 54.3, pp. 725–731.

Zierler, Kenneth L (1962). 'Theoretical basis of indicator-dilution methods for measuring flow and volume'. In: *Circulation Research* 10.3, pp. 393–407.

Appendix A

List of Publications by the Author

A.1 Conferences Presentations

1. Y. Hu, J. Huang, M. Muzi, F. OSullivan; "Parametric Imaging of DCE-MRI data: An Adaptation of a Mixture Analysis Scheme Used for Kinetic Mapping of Dynamic PET Data"; WMIC 2019, Montréal, Canada, September 4-7, 2019. [Poster Presentation]

2. Y. Hu, J. Huang, M. Muzi, F. OSullivan; "An Application of Mixture Analysis to Recover Local Kinetic Information from DCE-MRI Studies"; IEEE NIC MIC 2019, Manchester, UK, 26 October – 2 November, 2019. [Poster Presentation]

Appendix B

Nomenclature

B.1 Symbol Definitions

Symbol	Description	Unit
B_1	RF magnetic field component	
ω_0	Larmor frequency	Hz
γ	Gyromagnetic ratio of proton	MHz/T
B_0	Static magnetic field	T
T_1	Longitudinal (spin-lattice) relaxation time	ms
T_2	Transverse (spin-spin) relaxation time	ms
T_2^*	Actual transverse relaxation time	ms
TR	Repetition time	ms
TE	Echo time	ms
M_z	Longitudinal component of net magnetization	

M_0	Equilibrium magnetization	
M_{xy}	Transverse component of net magnetization	
r_1	Spin-lattice relaxivity constant	L/mmol·s
R_{10}	Normal spin-lattice relaxation rate	1/s
r_2	Spin-spin relaxivity constant	L/mmol·s
R^*_{20}	Normal spin-spin relaxation rate	1/s
$S(t)/S_0$	Relative MR signal intensity (normalized)	
$S(t)$	MR signal intensity	
S_0	Baseline signal intensity	
α	Concentration offset constant, $1/(r_1 T_{10})$	mmol/L
β	Concentration scale constants	
$Eht(t)$	Signal enhancement	
$C_b(t)$	Whole-blood concentration	mmol/L
$C_p(t)$	Plasma concentration	mmol/L
Hct	Hematocrit	
v_p	Plasma fractional volume	
$C_e(t)$	Concentration in the extracellular extravascular space (EES)	mmol/L
v_e	EES fractional volume	
$R(t)$	Residue function	
V_t	Total lesion tissue volume	mL
P	Vascular permeability	
S	Surface area of the leaky membrane	
F_b	Blood flow	mL/min/100mL
PS	Permeability surface area product	mL/min/100mL
ρ	Tissue density	g/mL

F_p	Plasma inflow rate	mL/min/100mL
v_f	Interstitial volume fractions of fast compartments	
v_s	Interstitial volume fractions of slow compartments	
τ_i	Intracellular water residence time	sec
R_{ie}	Relaxation rate for extracellular space	1/sec
R_{1i}	Relaxation rate for intracellular space	1/sec
T_o	Contrast arrival time	sec
TTP	Time-to-peak	sec
NEI	Negative enhancement integral	
MTE	Mean time to enhance	sec
MSD	Maximum signal drop	
MSI	Maximum signal increase	
k_h	Hematocrit correction factor	
TTP	Time to peak, $T_p - T_o$	sec
ΔS	Maximal contrast enhancement	
Wash-in Slope	Initial enhancement rate	sec^{-1}
Wash-out Slope	Contrast decay rate after peak	sec^{-1}
AUC	Area under the concentration-time curve	
$IAUC$	Initial area under the concentration-time curve	

B.2 Abbreviations

1D one-dimensional

2C two-compartment

2CXM two-compartment exchange model

2D two-dimensional

2SX two-site exchange

3C three-compartment

3D three-dimensional

ACRIN American College of Radiology Imaging Network

AI artificial intelligence

BALDERO
blood agent level-dependent and extravasation relaxation overview

BBB blood-brain barrier

BM Brix Model

CA contrast agent

CBF cerebral blood flow

CBV cerebral blood volume

CNS central nervous system

CRAN Comprehensive R Archive Network

CSF cerebrospinal fluid

CT computed tomography

CM cranial meninges

cSVD circular SVD

DCE-MRI dynamic contrast-enhanced magnetic resonance imaging

DFA dual-flip-angle

DICOM digital imaging and communications in medicine

DP Model distributed-parameter model

DSC-MRI dynamic susceptibility contrast magnetic resonance imaging

DWI diffusion-weighted imaging

EES extracellular extravascular space

EIS extravascular intracellular space

ETK Model
extended Tofts-Kermode model

FA flip angles

FDI free induction decay

FDA U.S. Food and Drug Administration

FLAIR Fluid-Attenuated Inversion Recovery

FOV field of view

FTT Fast Fourier Transform

GBM glioblastoma

GF glomerular filtration rate

GM grey matter

GRE gradient echo sequences

GVF gamma-variate function

IQRs interquartile ranges

IR inversion recovery

LL Look-Locker

LM Larsson Model

MCA middle cerebral artery

MM millimeters

MOLELI modified Look-Locker inversion recovery

MR magnetic resonance

MRI magnetic resonance imaging

MRS proton magnetic resonance spectroscopy

MSIR multi-slice inversion recovery sequence

MTT plasma mean transit time

NMR nuclear magnetic resonance

OLS ordinary least squares

oSVD oscillation SVD

PET positron emission tomography

PWI perfusion weighted image

PK pharmacokinetic

PM Patlak model

QIBA Quantitative Imaging Biomarkers Alliance

RF radiofrequency

RMSE root mean squared error

ROI regions of interest

RSS residuals sum of squares

SCR single compartment recirculation

SE spin echo

SNR signal-to-noise ratio

SPECT single photon emission computed tomography

SPGR spoiled gradient recall echo

SPICE spiral perfusion imaging with consecutive echoes

SSM shutter-speed model

SSS superior sagittal sinus

SVD singular value decomposition

TESO-IRFSE
time-efficient slice ordering inversion recovery fast spin echo

TH Model tissue homogeneity model

TCIA The Cancer Imaging Archive

TI inversion times

TK Model Tofts-Kermode model

VTF vascular transport function

WM white matter

fMRI functional MRI